Finding Transition State and Minimum Energy Path of Bistable Elastic Continua through Energy Landscape Explorations

Guangchao Wan[a,b,*], Samuel J. Avis[c,*], Zizheng Wang[d], Xueju Wang[d,e,ǂ], Halim Kusumaatmaja[c,ǂ], Teng Zhang[a,b,ǂ]

[a] Department of Mechanical and Aerospace Engineering, Syracuse University, Syracuse, NY 13244, USA

[b] BioInspired Syracuse, Syracuse University, NY 13244, USA

[c] Department of Physics, Durham University, Durham, DH1 3LE, England, United Kingdom

[d] Department of Materials Science and Engineering, University of Connecticut, Storrs, CT 06269, USA

[e] Institute of Materials Science, University of Connecticut, Storrs, CT 06269, USA

[*] These authors contribute equally to this work

[ǂ] Corresponding authors

Abstract

Mechanical bistable structures have two stable equilibria and can transit between them under external stimuli. Due to their unique behaviors such as snap-through and substantial shape changes, bistable structures exhibit unprecedented properties compared to conventional structures and thus have found applications in various fields such as soft robots, morphing wings and logic units. To quantitatively predict the performance of bistable structures in these applications, it is desirable to acquire information about the minimum energy barrier and an energy-efficient transition path between the two stable states. However, there is still a general lack of efficient methodologies to obtain this information, particularly for elastic continua with complicated, unintuitive transition paths. To overcome this challenge, here we integrate energy landscape exploration algorithms into finite element method (FEM). We first utilize the binary image transition state search (BITSS) method to identify the saddle point and then perform nudged elastic band (NEB) calculations with initial guess based on the BITSS results to find the minimum energy path (MEP). This integrated strategy greatly helps the convergence of MEP calculations, which are highly nonlinear. Two representative cases are studied, including bistable buckled beams and a bistable unit of mechanical metamaterials, and the numerical results agree well with the previous works. Importantly, we numerically predict the complicated MEP of an asymmetric bistable unit of mechanical metamaterials and use experiments to demonstrate that following this MEP leads to successful transition between stable states while intuitive uniaxial compression fails to do so. Our work provides an effective numerical platform for identifying the minimum energy barrier and energy-efficient transition path of a bistable continuum, which can offer valuable guidance to the design of actuators, damping structures, energy harvesters, and mechanical metamaterials.

Keywords: Bistable continuum structures; Binary image transition state search; Energy barrier; Minimum energy path; Nudged elastic band; Asymmetric Transition Path.

1. Introduction

Mechanical bistable structures abound in biological and artificial systems. For instance, Venus flytrap snaps from an "open" to a "closed" state to capture the prey (Forterre et al., 2005). A thin spherical cap can stay stable if flipped over (Holmes and Crosby, 2007; Taffetani et al., 2018; Wan et al., 2021). A laminate composite can bend towards two opposite sides caused by differential thermal strain between fibers and matrix (Daynes et al., 2008). Slender elastic structures can exhibit more than one stable shape owing to specific geometry or connection (Huang et al., 2022; Yu et al., 2021; Lu et al., 2023b, 2023a). The existence of two stable equilibria and the ability to transit between them driven by external stimuli endow bistable structures with distinguished static or dynamic properties and therefore make them potential candidates in various applications. To name a few, bistable structures can transform into new stable shapes that require no continuing energy input to maintain, thus being promising for many applications including energy-efficient morphing wings in aircraft (Arrieta et al., 2014; Boston et al., 2022; Diaconu et al., 2008; Mattioni et al., 2008; Rivas-Padilla et al., 2023), switches (Gomez et al., 2017a; Hou et al., 2018), logic units (Jiang et al., 2019; Meng et al., 2021; Pal and Sitti, 2023; Yan et al., 2023), grippers (C. Li et al., 2021; Power et al., 2023; Zhang et al., 2022), robots (Y. Li et al., 2021b), micro-electronics (Fu et al., 2018), origami-based structures (Dai et al., 2023; Faber et al., 2018; Fang et al., 2017; Li and Pellegrino, 2020; K. Liu et al., 2019; Lu et al., 2023c; Melancon et al., 2021; Silverberg et al., 2015; Yasuda and Yang, 2015) and valves (Preston et al., 2019; Qiao et al., 2021; Rothemund et al., 2018). By exploiting the conversion of stored potential energy to kinetic energy during snap-through instability, bistable designs increase the force output of actuators (Gorissen et al., 2020; Tian et al., 2021; Wang et al., 2023) and make unidirectional, self-supported wave propagation possible in mechanical metamaterials (Meaud and Che, 2017; Vasios et al., 2021; Xiu et al., 2022; Yasuda et al., 2020). In addition, when subjected to external impact, the transition from a lower energy state to the other stable state with higher energy can effectively absorb the energy of the impact, thereby reducing the peak force of the impact (Ghavidelnia et al., 2023; Restrepo et al., 2015; Shan et al., 2015). Furthermore, the inter-well vibration (periodic transition between two stable states) can broaden the working frequency of energy harvesters if bistable structures are combined with piezoelectric materials (Arrieta et al., 2013; Harne and Wang, 2013; Li et al., 2015).

To quantitatively evaluate the performance of bistable structures in these aforementioned applications, it is desired to survey their energy landscapes. Among various parameters, it is of particular importance to know the location of the saddle point and minimum energy path (MEP). Here, a saddle point, also known as transition state, is an equilibrium state that is unstable along certain directions (Wales, 2004). It is located at the "ridge" that separates two "valleys" in the energy landscape, representing two locally stable states. For the minimum energy path, it is a transition path that connects two stable states and passes through the saddle point. It is defined as the path whose tangent vector always keeps parallel to the gradient of the energy landscape and therefore serves as an energy-efficient transition route. Along this MEP, the saddle point corresponds to the highest energy state. However, this maximum energy along the MEP is lower than the highest energy along any other transition path. Therefore, the energy difference between the saddle point and locally stable state is the minimum energy barrier, which is the minimally required energy to complete the transition from one state to another. In some mechanical systems (Taffetani et al., 2018), there could be more than one saddle point between two stable states.

Therefore, multiple MEPs can exist, and each includes one saddle point (Bolhuis et al., 2002) and represents a locally energy efficient transition pathway.

The saddle point and the associated MEP that connects two stable states are paramount in estimating the performance of bistable structures in several aspects. For example, the minimum energy barrier can be used to characterize the stability and load-bearing capacity of each stable shape. The higher the barrier is, the more stable the state will be. Such a concept has already been adopted in analyzing the so-called "shock sensitivity" of a cylindrical shell subjected to buckling instability (Horák et al., 2006; Marthelot et al., 2017; Panter et al., 2019; Thompson et al., 2017; Virot et al., 2017). The calculated energy barrier also determines the energy output of actuators (Chi et al., 2022; Tang et al., 2020) and wave propagation speed in metamaterials (Deng et al., 2020; Jin et al., 2020; Vasios et al., 2021) when snap-through is utilized. In addition, the energy barrier decides the smallest amplitude of the external input to excite the inter-well vibration so that the bistable energy harvesters can have broadband collecting frequency (Arrieta et al., 2010; Liu et al., 2013; Pan, 2017). At the same time, since MEP always follows the gradient of the energy landscape, one could use its tangent vector to derive the necessary, general external force along the transition path, providing valuable guidance to shape transformation of bistable structures. Therefore, establishing a general and efficient method to search for the saddle point and MEP will be beneficial to not only academic interests but also practical purposes.

Intensive studies have been reported on the energy landscape analysis of bi-stable elastic structures. For example, arc-length methods have been widely used for snap-through instability analysis and shown to successfully capture the saddle point along certain chosen loading path and keep track of an unstable branch (Champneys et al., 2019; Crisfield, 1981; Eriksson, 1998; Groh et al., 2018; Liu et al., 2017; Y. Liu et al., 2019; Riks, 1979; Wan et al., 2021). However, the path identified by this method is associated with the prescribed forms of external force and thus may not be the MEP. In recent years, there have been efforts in integrating numerical methods in the fields of physics and chemistry, traditionally used to study chemical reaction, phase transition, nucleation, and other rare events (e.g., Garrido Torres et al., 2019; Henkelman et al., 2000; Henkelman and Jónsson, 2000), into mechanical modeling to capture the saddle point and MEP. To name a few, Panter, et al. (Panter et al., 2019) combined the string method with the triangulated lattice model to search for the saddle point and the minimum energy path (MEP) of a cylindrical shell under axial loading to control its buckling behaviors. Zhou, et al. (Zhou et al., 2023) used the nudged elastic band (NEB) method together with the truss-based approach to find the efficient transition path of origami panels. Song, et al. (Song et al., n.d.) employed the conjugate peak refinement method to search for the transition path of multi-stable tensegrity structures. Avis, et al. (Avis et al., 2022) developed a binary image transition state search (BITSS) algorithm to efficiently capture the saddle point of a buckling cylindrical shell based on the triangulated lattice model. This was initially used by Li, et al. (Y. Li et al., 2021a) who integrated this BITSS method together with the string method into a discretized shell model to find the saddle point and MEP of a multi-stable ferromagnetic meso-structures. Although great process has been made, the previous works on the elastic continua mostly adopted certain mechanical models such as shell model that target slender structures, whereas the application of these energy landscape exploration methods on bistable elastic continua based on a more general mechanical framework has not been explored.

In this work, by integrating the binary image transition state search (BITSS) and nudged elastic band (NEB) method into finite element method (FEM) that is widely used for modeling elasticity continua, we introduce a general numerical framework that can efficiently capture the saddle point and MEP of bistable elastic continua. Specifically, we first use the BITSS method that manipulates only two “images” to locate the saddle point. Here the term “image” refers to a full set of nodal spatial coordinates of the meshed elastic structures that satisfies the displacement boundary conditions. Based on the BITSS results, we then employ gradient descent method to generate an initial guess for the NEB method that can successfully find the minimum energy path (MEP). The combination of these two algorithms greatly improves the convergence of MEP calculations, which are highly nonlinear, with cheap computational cost. The proposed computational pipeline has been tested on two representative cases, which are bistable buckled beams and bistable units of mechanical metamaterials. Our results are in great agreement with experimental validations of bistable units of mechanical metamaterials and the previous works. It is worth pointing out, as will be presented later in this paper, that our methodology is capable of identifying asymmetric transition pathways that are difficult to achieve through intuition.

The rest of the paper is organized as follows. Section 2 presents BITSS and NEB algorithms using a 2D bistable von-Mises truss system as an example and briefly describes their integration into finite element method (FEM) based on 2D plane strain problems. The saddle point and MEP of a bistable buckled beam with two rotational ends are discussed in Section 3 in two scenarios: two stable states have the same or different elastic energy. Section 4 is dedicated to the analysis of the energy landscape of a bistable unit of mechanical metamaterials with symmetric or asymmetric, unintuitive MEP. Finally, some concluding remarks are given in Section 5.

2. Illustrations of energy landscape exploration algorithms

We start with a simple bistable case, a 2D bistable von-Mises truss, to illustrate both BITSS and NEB algorithms. Such a bistable mechanism has been broadly employed in metamaterials (Chen et al., 2017; Shan et al., 2015), deployable structures in aerospace (Schioler and Pellegrino, 2007), etc. As shown in Figure 1(a), the von-Mises truss consists of two rigid bars connected by a free hinge A. The two bars have lengths l_1 and l_2, respectively. The other ends of the two bars are located at the same horizontal line (x axis) and can only slide along the horizontal direction under the constraints of two linear springs with spring stiffnesses k_1 and k_2 and two torsional springs with stiffnesses $k_{\theta,1}$ and $k_{\theta,2}$. The rotational angles of the two bars compared to the horizontal direction are denoted as θ_1 and θ_2. The system has two degrees of freedom (DoF), including the x and y position of the point A. Initially, all springs are at their rest and point A is located at (0, h). In addition to this stress-free shape that is denoted as S_1, the von-Mises truss has another self-stressed, inverted shape denoted as S_2. The potential energy E and its gradient with respect to the DoF of the system have analytical expressions as

$$E = \frac{1}{2}k_1\left(x - l_1cos\theta_1 + l_1cos\theta_{1,r}\right)^2 + \frac{1}{2}k_2\left(-x - l_2cos\theta_2 + l_2cos\theta_{2,r}\right)^2 + \frac{1}{2}k_{\theta,1}\left(\theta_1 - \theta_{1,r}\right)^2 + \frac{1}{2}k_{\theta,2}\left(\theta_2 - \theta_{2,r}\right)^2$$

(Eq. 2.1)

$$\frac{\partial E}{\partial x} = k_1\left(x - l_1cos\theta_1 + l_1cos\theta_{1,r}\right) + k_2\left(x + l_2cos\theta_2 - l_2cos\theta_{2,r}\right)$$

$$\frac{\partial E}{\partial y} = \frac{k_1\left(x - l_1cos\theta_1 + l_1cos\theta_{1,r}\right)l_1sin\theta_1}{\sqrt{{l_1}^2 - y^2}} + \frac{k_2\left(-x - l_2cos\theta_2 + l_2cos\theta_{2,r}\right)l_2sin\theta_2}{\sqrt{{l_2}^2 - y^2}} + \frac{k_{\theta,1}\left(\theta_1 - \theta_{1,r}\right)}{\sqrt{{l_1}^2 - y^2}} + \frac{k_{\theta,2}\left(\theta_2 - \theta_{2,r}\right)}{\sqrt{{l_2}^2 - y^2}}$$

(Eq. 2.2)

where $\theta_{1,r}$ = arcsin(h/l_1) and $\theta_{2,r}$ = arcsin(h/l_2) are the rotational angles of the two bars when the springs are at rest. In a specific case, we choose parameters as l_1 = 5 mm, l_2 = 7 mm, h = 3.5 mm, k_1 = 0.1 N/mm, k_2 = 0.08 N/mm, $k_{\theta,1}$ = 0.1 J/rad and $k_{\theta,2}$ = 0.08 J/rad and plot the contour of the energy landscape based on Eq. 2.1&2.2 (Figure 1(b)). Two stable states have the elastic energy as E_{S_1} = 0 J and E_{S_2} = 0.148 J and sit at the bottom of the "valley", separated by a mountain "ridge". The minimum energy path (MEP) connects these two states and goes through the saddle point that is located between two "valleys". The saddle point has an elastic energy as E_T = 0.173 J. The energy difference between the saddle point and the stable state is the minimum energy barrier that we seek, which is 0.025 J if the structure transition from the state S_2 to state S_1. To highlight its importance, let us suppose a simple transition path that directly connects two stable states in the coordinate space (*x*,*y*) (line *P*, Figure 1(b)), which can be realized by indentation in experiment. However, such a simple path will lead to a higher energy barrier as 0.032 J compared to MEP that goes through the saddle point *T* (Figure 1(c)).

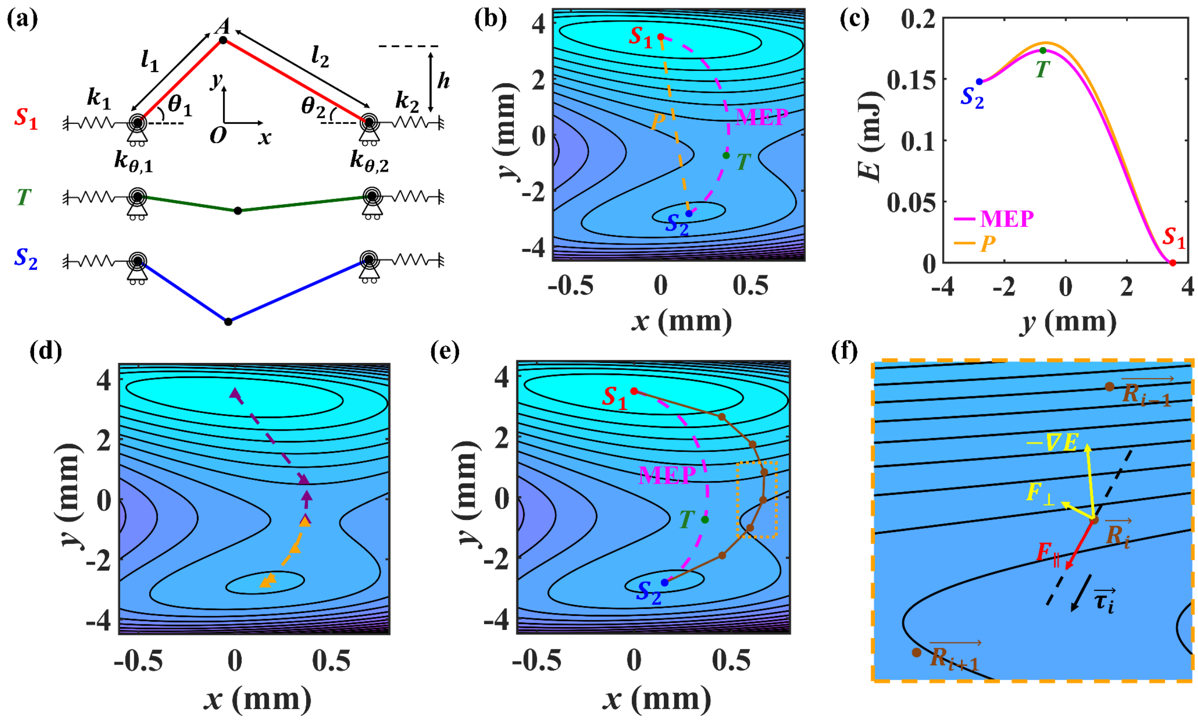

Figure 1. (a) Schematic illustration of the two stable states S_1 and S_2 and the transition state T of a von-Mises truss. The parameters are chosen as l_1 = 5 mm, l_2 = 7 mm, h = 3.5 mm, k_1 = 0.1 N/mm, k_2 = 0.08 N/mm, $k_{\theta,1}$ = 0.1 J/rad and $k_{\theta,2}$ = 0.08 J/rad. (b) The energy landscape of the von-Mises truss. The red (S_1) and blue (S_2) circles represent the locations of the stable states. The green circle is the location of the saddle point (T). The dash pink curve is the MEP while the straight orange line is an indentation path. (c) Comparison of the energy variation along the MEP and the orange indentation line. (d) The iterative process of two images during the BITSS algorithm. Triangles represent the locations of the images while the dash line is for better visualization. (e) Illustrations of the string of images (brown circles) in the NEB method. (f) Zoom-in of three adjacent images $\boldsymbol{R_{i-1}}$, $\boldsymbol{R_i}$ and $\boldsymbol{R_{i+1}}$ (brown) in (e), in which the tangent vector $\boldsymbol{\tau_i}$ (black), the parallel and perpendicular components of the force $F_{\parallel}$ (red) and $F_{\perp}$ (yellow) are illustrated.

2.1. Binary Image Transition State Search (BITSS) Method

To efficiently capture the saddle point, we adopt the binary image transition state search (BITSS) method that has recently been introduced by Avis, et al. (Avis et al., 2022). They have also shown that BITSS is more reliable compared to other bracketing methods, where two images are manipulated until they converge to the saddle point. Compared to double-ended chain-of-states methods that can require a chain of more than ten intermediate states, BITSS is computation- and memory-efficient since it only involves two images. In addition, BITSS is less sensitive to initialization while an appropriate interpolation is commonly needed as an initial pathway estimate for conventional double-ended algorithms. This is particularly an issue for elastic structures where interpolations can lead to a large amount of internal stress, which can cause numerical issues such as converging to an incorrect pathway or divergence. Therefore, for a bistable elastic body with a complicated transition path, BITSS can be a general and effective method to locate the saddle point. Additionally, the amenability of BITSS to adaptive remeshing could allow integration with commonly used adaptive finite element methods, however this will not be explored within this work.

Specifically, we study a mechanical system whose elastic energy E is a scalar function of n DoF as $E = E(\boldsymbol{X})$, in which $\boldsymbol{X} = [x_1; x_2; \dots; x_n]$ is the n-dimensional space of the system. Particularly, in this study, the components of $\boldsymbol{X}$ take the Cartesian coordinates of n/2 nodes in the two-dimensional (2D) mesh structures. In this n-dimensional space $\boldsymbol{X}$, the column vectors $\boldsymbol{S_1}$ and $\boldsymbol{S_2}$ represent the two stable states while the vector $\boldsymbol{T}$ represents the saddle point (transition state). BITSS is initiated with two images $\boldsymbol{X_1}$ and $\boldsymbol{X_2}$ sitting in two basins of attraction that are separated by a "ridge". As mentioned, each image can represent an arbitrary state in the n-dimensional space as long as its components conform to the prescribed boundary conditions. These two images in the initial stage can be chosen as stable states $\boldsymbol{S_1}$ and $\boldsymbol{S_2}$, but it is not necessarily required. To make the two images converge to the saddle point, BITSS minimizes the total energy of two images together with two constraints on the Euclidean distance between the two images and their energy difference. These constraints ensure that neither image can cross over the "ridge" and slide to one of the local minima. Thus, the total energy in BITSS algorithm is written as

$$E_{BITSS}(\boldsymbol{X_1}, \boldsymbol{X_2}) = E_1(\boldsymbol{X_1}) + E_2(\boldsymbol{X_2}) + k_e[E_1(\boldsymbol{X_1}) - E_2(\boldsymbol{X_2})]^2 + k_d[d(\boldsymbol{X_1}, \boldsymbol{X_2}) - d_i]^2$$

(Eq. 2.3)

where E_1 and E_2 are the elastic energy of two states and k_e and k_d are spring stiffness that measures the strengths of distance and energy difference constraints, d is the Euclidean distance between two images $d = \|\boldsymbol{X_1} - \boldsymbol{X_2}\| = \sqrt{(\boldsymbol{X_1} - \boldsymbol{X_2}) \cdot (\boldsymbol{X_1} - \boldsymbol{X_2})}$ and d_i is constrained distance specified at the i-th iteration that is incrementally reduced as $d_i = (1 - f)d_{i-1}$ in which $0 < f < 1$ is the reduction factor for the constrained distance.

In Eq. 2.3, the BITSS energy E_{BITSS} is a scalar function of two images $\boldsymbol{X_1}$ and $\boldsymbol{X_2}$. Therefore, its DoF is twice of the system's DoF. At each iteration, under the specified constrained distance d_i, we minimize the BITSS energy E_{BITSS} through finding the zeros of its gradient ∇E_{BITSS} regarding the column vector $[\boldsymbol{X_1}; \boldsymbol{X_2}] = \left[x_{1,1}; x_{1,2}; \dots; x_{1,n}; x_{2,1}; x_{2,2}; \dots; x_{2,n}\right]$ where $x_{i,j}$ is the j-th DoF of the i-th image as

$$\nabla E_{BITSS} = \nabla E_1 + \nabla E_2 + 2k_e(E_1 - E_2)(\nabla E_1 - \nabla E_2) + 2k_d(d - d_i)\nabla d$$

(Eq. 2.4)

Specifically, we resort to the root-finding function *fsolve* in MATLAB to calculate the zeros of the gradient ∇E_{BITSS}. During the minimization, it is desired that the magnitude of each term in Eq. (2.4) is relatively the same to guarantee a successful search. As a result, we keep updating the values of k_e and k_d every three calling of the BITSS energy E_{BITSS} based on the following formula (Avis et al., 2022)

$$k_e = \frac{\alpha}{2E_B}$$

(Eq. 2.5)

$$k_d = max\left(\frac{\sqrt{\|\nabla E_1\|^2 + \|\nabla E_2\|^2}}{2\sqrt{2}\beta d_i}, \frac{E_B}{\beta {d_i}^2}\right)$$

(Eq. 2.6)

where E_B is the estimated energy barrier between two images and α and β are two parameters. The estimated energy barrier E_B is calculated as the difference between the highest energy along a linear interpolation of two images and the average energy of two images. It is worth mentioning here that for mechanical systems with multiple saddle points, minimization of the BITSS energy E_{BITSS} typically reaches the saddle point with the lowest energy barrier because the expression (Eq. 2.3) contains the energy of two images.

For the bistable von-Mises truss, the two images are initiated as the two stable states, and the parameters are set as f = 0.5, α = 10 and β = 0.1, as recommended by previous work (Avis et al., 2022). However, as will be shown later, it may be necessary to tune the α and β parameters to prohibit the image initiated in the valley with higher energy (hence lower energy barrier) from crossing over the ridge. As shown in Figure 1(d) for the bistable von-Mises truss, the two BITSS images gradually approach each other and successfully converge at the saddle point. It is worth mentioning that in this case the trajectories of two images during iterations are close to the MEP, however, it is not a general behavior for most cases (Avis et al., 2022), as will be shown later in Figure 8(d). Therefore, it is necessary to employ a new numerical algorithm to find the MEP.

2.2. Nudged Elastic Band (NEB) Method

Once we successfully pinpoint the saddle point, we employ the nudged elastic band (NEB) algorithm to search the MEP accordingly. The NEB is a popular two-ended method that has been widely used in calculating the diffusion process, dislocation, solid-solid transformation and chemical reaction (Ásgeirsson et al., 2021; Bohner et al., 2014; Chen et al., 2019; Garrido Torres et al., 2019; Ghasemi et al., 2019; Ghasemi and Gao, 2020; Kolsbjerg et al., 2016; Rao et al., 2011; Sheppard et al., 2012; Si et al., 2023; Sobie et al., 2017; Xie et al., 2004). Here we give a brief review of the NEB algorithm and refer readers to previous works for the details of the method (Henkelman et al., 2000; Henkelman and Jónsson, 2000; Trygubenko and Wales, 2004). In the NEB algorithm, a string of *N* images $[\boldsymbol{R_1}; \boldsymbol{R_2}; \dots; \boldsymbol{R_N}]$, in which the column vector $\boldsymbol{R_i}$ denotes to the *i*-th image with *n* DoF, is used to represent the transition path in a discretized manner, and the two stable states are always the first and last images $\boldsymbol{R_1}$ and $\boldsymbol{R_N}$, respectively. Meanwhile, the rest images are allowed to move. Each image is connected to its adjacent two images through an elastic band with spring stiffness k_{NEB}. As the algorithm advances, these *N* images are gradually relaxed from the initial interpolation between two stable states to the MEP through reducing the exerted force of each image to zero. On the *i*-th image $\boldsymbol{R_i}$, the exerted force can be divided into a parallel and perpendicular component based on the tangent direction of this image $\boldsymbol{\tau_i}$, as shown in Figure 1(f). Along the parallel direction, the force is provided by the elastic band only with the equation

$$F_{\parallel} = k_{NEB}(\|\boldsymbol{R_i} - \boldsymbol{R_{i-1}}\| - \|\boldsymbol{R_{i+1}} - \boldsymbol{R_i}\|)$$

(Eq. 2.7)

When the parallel force $F_{\|}$ is reduced to zeros, it guarantees that the images are distributed uniformly along the transition path to well represent the MEP. Here, we further utilize the image climbing technique on the image with the highest energy along the string $\boldsymbol{R}_{\boldsymbol{i}_{max}}$ (Henkelman et al., 2000) to capture the saddle point and compare it to the BITSS results for consistency. For this image $\boldsymbol{R}_{\boldsymbol{i}_{max}}$, its parallel force takes the form of the inverted parallel component of the energy landscape gradient as $-\nabla E\left(\boldsymbol{R}_{\boldsymbol{i}_{max}}\right) + 2\left[\nabla E\left(\boldsymbol{R}_{\boldsymbol{i}_{max}}\right) \cdot \boldsymbol{\tau}_{\boldsymbol{i}_{max}}\right]\boldsymbol{\tau}_{\boldsymbol{i}_{max}}$ instead of Eq. 2.7. Driven by this force, this image will climb uphill to find the saddle point.

For the perpendicular component $F_{\perp}$, it comes from the projection of the force $-\nabla E(\boldsymbol{R}_{\boldsymbol{i}})$ along the direction perpendicular to the tangent vector $\boldsymbol{\tau}_{\boldsymbol{i}}$ as $-\nabla E(\boldsymbol{R}_{\boldsymbol{i}}) + [\nabla E(\boldsymbol{R}_{\boldsymbol{i}}) \cdot \boldsymbol{\tau}_{\boldsymbol{i}}]\boldsymbol{\tau}_{\boldsymbol{i}}$ (Figure 1(f)). Since the MEP always follows the energy landscape gradient, the reduction of the perpendicular component $F_{\perp}$ to zero ensures that the string of images converges to the MEP. To incrementally decrease the force magnitude, we utilize the *fsolve* function in MATLAB.

The implementation of NEB relies on an accurate estimation of the tangent vector. Here, for the *i*-th image $\boldsymbol{R}_{\boldsymbol{i}}$, its tangent vector $\boldsymbol{\tau}_{\boldsymbol{i}}$ is estimated based on its two adjacent images as

$$\boldsymbol{t}_{\boldsymbol{i}} = \frac{\boldsymbol{R}_{\boldsymbol{i}} - \boldsymbol{R}_{\boldsymbol{i-1}}}{\|\boldsymbol{R}_{\boldsymbol{i}} - \boldsymbol{R}_{\boldsymbol{i-1}}\|} + \frac{\boldsymbol{R}_{\boldsymbol{i+1}} - \boldsymbol{R}_{\boldsymbol{i}}}{\|\boldsymbol{R}_{\boldsymbol{i+1}} - \boldsymbol{R}_{\boldsymbol{i}}\|}$$

$$\boldsymbol{\tau}_{\boldsymbol{i}} = \frac{\boldsymbol{t}_{\boldsymbol{i}}}{\|\boldsymbol{t}_{\boldsymbol{i}}\|}$$

(Eq. 2.8)

Though powerful, the NEB method may have difficulty in converging especially when the energy landscape is complicated. The convergence of the NEB calculation is sensitive to the initial guess of the string of the images. To resolve this issue, we utilize the saddle point calculated from BITSS to provide a good initialization (Avis et al., 2022; Y. Li et al., 2021a). Specifically, we apply the gradient descent (GD) algorithm twice with each beginning with one of the two images in the last iteration from the BITSS results. As a result, the "slide-down" from the saddle point to both stable states can be captured, and the intermediate states during the GD algorithm are chosen as the initial guess for the string of images. Following this initialization strategy and choosing the parameters as $N = 12$ and $k_{NEB} = 0.1$ N/mm, we successfully capture the MEP of the bistable von-Mises truss as shown in Figure 1(e), in which the continuous MEP is obtained through the spline-interpolation of the images.

2.3. Integration of BITSS and NEB into FEM

The proposed computational framework has been verified in a sample bistable case with two degrees of freedom (DoF). To demonstrate its capability in capturing the saddle point and MEP in elastic continua with large numbers of DoF, we integrate BITSS and NEB algorithms into finite element method (FEM) that is broadly adopted to model the elastic behaviors of solids. For simplicity, we focus on 2D plane strain problems in which the elastic domain is discretized into linear triangular meshes. In FEM, the DOF are the nodal spatial coordinates of the triangular meshes. For a total number of nodes n_{FEM}, we assemble the nodal coordinates into a $2n_{FEM}$ multi-dimensional image $\boldsymbol{X}$ as $\boldsymbol{X} = [\overline{x_1}; \overline{y_1}; \overline{x_2}; \overline{y_2}; \dots; \overline{x_{n_{FEM}}}; \overline{y_{n_{FEM}}}]$ where $\overline{x_i}$ and $\overline{y_i}$ are the x- and y-coordinate of the i-th node. For the material property, we assign a hyper-elastic model with the strain energy density U written as

$$U = \frac{1}{2}\mu[tr(\boldsymbol{F}^T\boldsymbol{F}) - 2] - \mu ln[\det(\boldsymbol{F})] + \frac{1}{2}\lambda\{ln[\det(\boldsymbol{F})]\}^2$$

(Eq. 2.9)

where μ and λ are the shear modulus and Lame constants, respectively and $\boldsymbol{F}$ is the deformation gradient tensor in plane strain situations. By integrating the strain energy density over one element and assembling the strain energy of all elements together, one can calculate the total elastic energy of the structure $E(\boldsymbol{X})$ and its gradient $\nabla E(\boldsymbol{X})$ with respect to the image $\boldsymbol{X}$, which are necessary input for BITSS and NEB algorithms. For prescribed boundary conditions, special treatment is required for the nodes that are located at these boundaries. Here, for simplicity, we only focus on the displacement boundary conditions. For nodal coordinates that are constrained, the components of the force $-\nabla E$ along these DoF are assigned to be zeros so that these nodes do not move along certain direction as the algorithms proceed.

3. Bistable Buckled Beam with Clamped Rotational Ends

In this section, we utilize a bistable buckled beam with two rotational ends to demonstrate the capability of the introduced numerical platform. Extensive studies have been performed to investigate the mechanical behaviors of this bistable system such as its static behaviors and dynamic snap-through. G. Wan, et al. established the stability diagram of the bistable buckled beam in terms of the rotational angles of two clamped ends (Wan et al., 2019). M. Gomez, et al. studied the effect of the clamped angles on the bifurcation type of bistable beams and demonstrated the existence of the critical slowing down phenomenon during the dynamic snap-through when the buckled beam undergoes saddle-node bifurcation (Gomez et al., 2017b). T. Sano, et al. investigated the bistability of the buckled beam with frictional contact (Sano et al., 2017) or pinned boundary condition (Sano and Wada, 2018). A. Abbasi, et al. employed arc-length method to study the transition path of a bistable buckled beam that responds to magnetic field (Abbasi et al., 2023). R. Wiebe, et al. utilized the dynamic transition between two stable states to capture the saddle point (Wiebe and Virgin, 2016). B. Radisson, et al. examined the dynamic snap-through under symmetric boundary condition (Radisson and Kanso, 2023). By controlling the shape transition through external stimuli such as magnetic field, bistable beams can be applied as smart switches in electric circuits (Hou et al., 2018) or logic units for information operation (Pal and Sitti, 2023). The results based on these previous investigations make the bistable buckled beam an ideal candidate to verify our computational methods. Although existing beam theory (Liu et al., 2021; Zhang et al., 2020) or discrete elastic rod method (Huang et al., 2023) can accurately predict behaviors of buckled beams, we use FEM in the current paper since it can work for general elastic solids. The integration of BITSS and NEB algorithms into these beam models will be explored in future studies.

As schematically shown in Figure 2(a), a straight beam with two clamped ends has its thickness t = 2 mm and original length L = 100 mm. The parameters of the material property are chosen to be μ = 1 MPa, λ = 3 MPa. The geometric domain is discretized into triangular meshes. The mesh sizes are 1 and 0.5 along the length and thickness direction of the beam, respectively. After an axial compression, the distance between two ends becomes l, and the beam becomes bistable by buckling either upwards (S_1) or downwards (S_2). The compressive strain is defined as $\varepsilon_c = (L-l)/L$. It is the well-known Euler buckling instability. To facilitate the analysis, we build a Cartesian coordinate whose origin is located at the center of the un-deformed beam and the x axis is parallel to the centerline of the un-deformed beam.

If the two clamped ends do not rotate after the compression (ϕ_1 = 0°, ϕ_2 = 0°), the two buckled shapes are mirror symmetry to each other with respect to the x axis (Figure 2(b)). In addition, if we plot the elastic energy E of the beam versus the y coordinate of the beam's center y_c along the MEP, the energy landscape also contains mirror symmetry and the two shapes have the same elastic energy, since two buckling directions are equally preferred (Figure 2(b)). In this situation, the energy landscape is termed as symmetric.

To control the bistable behaviors and the energy landscape of the buckled beam, one can rotate the two clamped ends (Wan et al., 2019). For instance, as shown in Figure 2(c), by rotating the right end clockwise and keeping the left end unchanged (ϕ_1 = 0°, ϕ_2 = 5°), the elastic energy of the upwards shape (S_1) decreases while the energy of the downwards shape (S_2) increases, breaking the mirror symmetry of both configurations and the energy landscape. Due to the end rotation, the state S_1 is energetically preferred with a lower energy and a higher energy barrier and the state S_2 becomes "metastable" with a higher energy and lower energy barrier. Accordingly, the energy landscape becomes asymmetric. Both symmetric and asymmetric energy landscapes will be examined through our exploration algorithms.

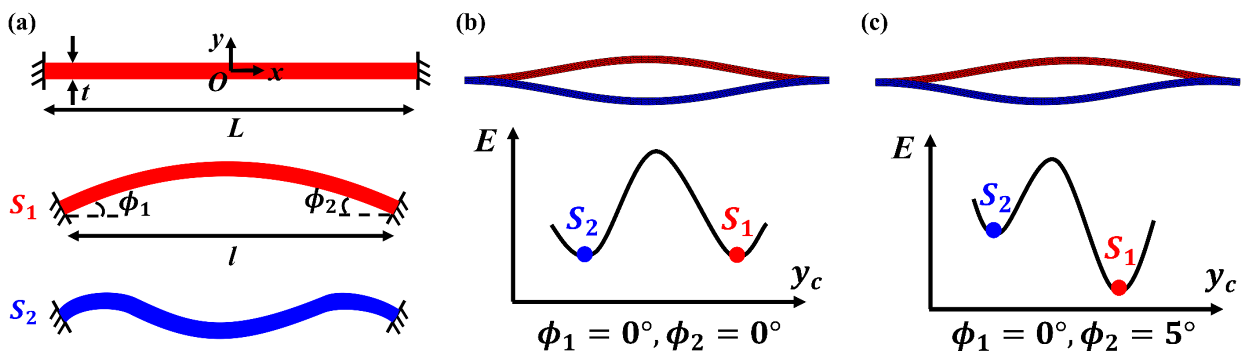

Figure 2. (a) Schematic illustration of the geometry of a buckled beam and two stable shapes that bend either upwards (S_1, red) or downwards (S_2, blue). (b) Mirror symmetry of two stable shapes and the corresponding energy landscape when two ends do not rotate (ϕ_1 = 0°, ϕ_2 = 0°). (c) Two stable shapes of the buckled beam with asymmetric energy landscape when one end rotates counterclockwise (ϕ_1 = 0°, ϕ_2 = 5°). In (b) and (c), the red color denotes to S_1 while the blue denotes to S_2.

3.1. Symmetric Energy Landscape

Asymmetric Transition Path

We first explore the energy landscape of a bistable buckled beam when its two ends do not rotate after compression. The compressive strain ε_c is set as 1%. In this situation, the two stable shapes are symmetric with respect to both *x* and *y* axes. To pinpoint the saddle point, the BITSS algorithm is first employed whose initiation is chosen as the two stable states. In the simulation, we set the distance rescaling parameter *f* = 5% and the algorithm stops when the distance between two images *d* is below 5% of its initial value. The values of two parameters α and β are chosen as α = 10, β = 0.1.

The shapes of two images as the algorithm proceeds are shown in Figure 3(a), in which the solid red and blue beams represent the two stable states S_1 and S_2 while the purple and orange shapes with meshes are two images during this iterative process. Initially, the two images hold the mirror symmetry as the measured distance between two images is close to that between two stable states after five iterations. However, as the iteration continues and the distance between the two images is shortened, the mirror symmetry is broken, and the two images become sinusoidal. This behavior agrees with the previous experimental and numerical efforts on the point indentation of a buckled beam (Harvey and Virgin, 2015). In the end, the distance between two images will be below 5% of the initial distance and we take the average of the two images as the approximation of the saddle point. The saddle point takes the sinusoidal shape with its center located at (0,0). Intuitively, the system keeps invariant under the mirror reflection based on *y* axis, suggesting that there should be another saddle point that is symmetric to the current one regarding *y* axis. However, the current triangular mesh introduces numerical bias to the ideally mirror symmetry so that two images do not converge to the other saddle point. To converge to such a saddle point, one could simply reverse the stacking direction of the triangular meshes.

In addition to the shapes, we also show the variation of the energy of two images during the iterative process and compare them with the true MEP. This can be obtained from high resolution NEB method (see below). Specifically, we choose the *y* coordinate of the beam's center y_c and the total elastic energy of the beam *E* to present the iterative results. As shown in Figure 3(b), two images gradually climb uphill in the energy landscape and approach the saddle point as BITSS algorithm proceeds. By averaging two images in the last step, we find the saddle point (green asterisk) at the highest point along the MEP, demonstrating the accuracy of the BITSS method. In Figure 3(c), we output the variation of two spring stiffness values k_e and k_d in the BITSS method as the iteration proceeds to better understand the BITSS method. As the algorithm continues, k_e keeps increasing and spans multiple orders of magnitude, since the estimated energy barrier between two images becomes smaller when the two images approach the saddle point (Eq. 2.5). At the same time, k_d undergoes a non-monotonic change within the same order of magnitude, because the energy gradient also lowers as the distance between two images decreases, effectively cancelling out changes to k_d (Eq. 2.6).

After finding the saddle point using the BITSS method, we apply the gradient descent (GD) algorithm to initiate the NEB calculation. To accelerate the calculation, we start with a low number of images ($N = 5$) and the spring stiffness k_{NEB} is set as $k_{NEB} = 1\times10^{-5}$ N/mm. As shown in Figure 3(d), the string of five images in NEB gradually moves and converges to the MEP. We then increase the number of images by linearly interpolating the current results as the initial guess for NEB calculation. Specifically, we add a new image between each pair of adjacent images, and the value of this new image is the average of two existing images. For instance, using NEB results with 5 images, we can add 4 more new images and construct initial guess for NEB algorithm with 9 images based on this interpolation technique, and the results are shown in Figure 3(e), where the images are sequentially arranged from top (S_1) to bottom (S_2). Following the MEP, the bistable buckled beam breaks its mirror symmetry and becomes sinusoidal, similar to the point indentation process of the beam's center (Harvey and Virgin, 2015). Finally, we increase the number of images N to 17 by constructing the initial guess through the same interpolation method and display the MEP in terms of the y coordinate of the beam's center y_c and the elastic energy E in Figure 3(f). The image of the highest energy overlaps with the saddle point from the BITSS calculation, suggesting that the NEB and BITSS algorithms converge to the same saddle point. Apart from the MEP, we also apply a mechanical indentation on the middle point of the beam's centerline through displacement control and compare it with the MEP. As shown in Figure 3f, the indentation passes through the saddle point, yet it is slightly different from the MEP. Based on the obtained MEP, the stable states S_1 and S_2 have the same energy as $E_{S_1} = E_{S_2} = 0.0113$ mJ while the saddle point T has the energy as $E_T = 0.0204$ mJ, leading to an energy barrier as 0.0091 mJ.

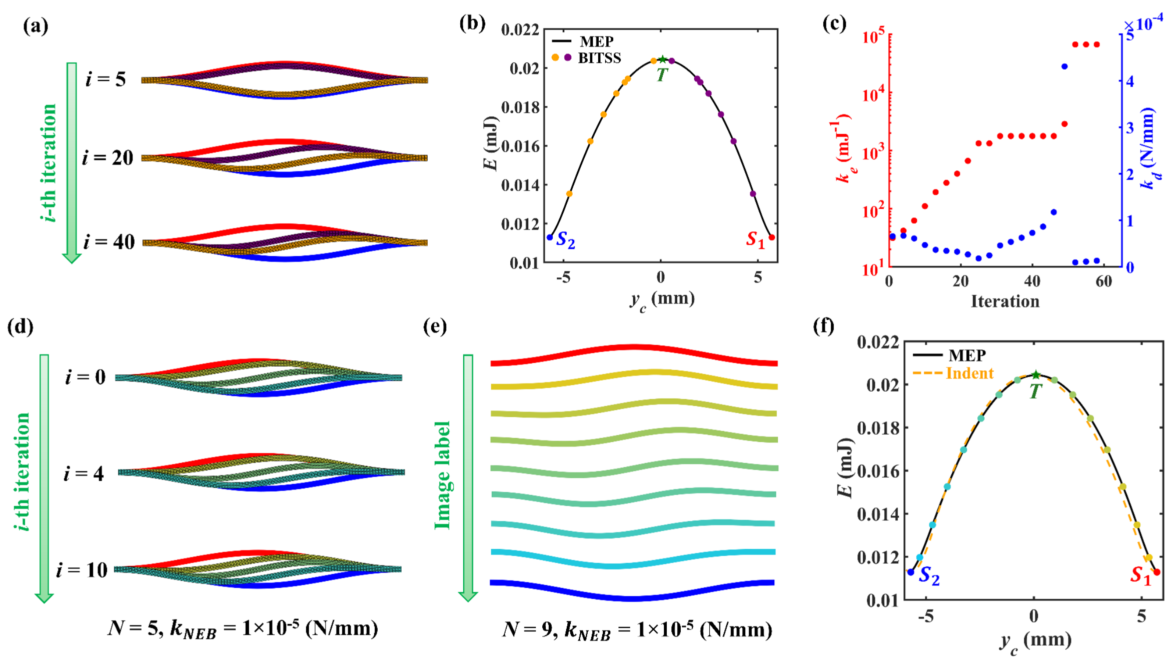

Figure 3. The asymmetric transition path for a buckled beam with $\varepsilon_c = 1\%$, $\phi_1 = \phi_2 = 0°$. (a) The shapes of the two images during iterations in the BITSS method. (b) The variation of the energy of the two images every five iterations in the BITSS method. (c) The variation of the spring stiffness k_e and k_d in the BITSS method every three iterations. (d) The shapes of five images during iterations in the NEB method with spring stiffness $k_{NEB} = 1\times10^{-5}$ N/mm. (e) The shapes of the 9 images when the NEB method converges. (f)

The MEP based on a spline-interpolation of 17 images from the NEB results in terms of y_c and E. In all figures, the red and blue color represent S_1 and S_2, respectively. The green asterisk is the saddle point by averaging the two images of the last iteration in the BITSS method. The purple and orange color denote to the two images in the BITSS method. The black curve is the MEP, and the orange dash line is the mechanical indentation.

Symmetric Transition Path

Apart from the asymmetric transition path in which the buckled beam becomes sinusoidal, the buckled beam can also follow a symmetric transition path passing through a saddle point with symmetric configuration. Such a symmetric transition path can be revealed in experiments by indenting a clamped beam with symmetric constraint (Neville et al., 2020, 2018) or with axial strain that is close to the Euler's buckling strain (Pandey et al., 2014). To prove the versatility of the proposed numerical framework, we also capture this symmetric transition path. In this situation, this symmetric saddle point contains higher elastic energy than the sinusoidal saddle point and hence a direct implementation of BITSS algorithm does not find such a symmetric configuration. Therefore, we prevent the middle section of the beam (x = 0) from any displacement along x direction to force the beam to stay in mirror symmetry with respect to y axis during the transition.

Under the symmetric constraint, the iterative process of BITSS is shown in Figure 4(a). Initially, as the distance between two images decreases, two images contain mirror symmetry to each other regarding the x axis. However, near the end of the iterations, the image that starts from the state S_2 (bottom, orange) flips from bending downwards to upwards. This change is also clearly shown in the energy variation of two images along the MEP. As shown in Figure 4(b), when two images get close to the saddle point (green asterisk), one image deviates from the MEP slightly while the other image still follows the MEP as the iteration proceeds. This behavior is caused by the fact that the saddle point in this situation is cosine-like rather than being straight – the beam favors bending instead of an axial compression to lower its elastic energy even under the symmetric constraint (Figure 4(a)). Therefore, the mirror symmetry between two images with respect to the x axis initially needs to be broken near the end of the iterations.

The NEB results with 7 images are shown in Figure 4(c). Along the MEP from the stable shape that bends upwards (S_1, red) to downwards (S_2, blue), the buckled beam keeps its bending direction in its middle part yet flips its bending direction near two ends before reaching the saddle point. However, after passing the saddle point, the buckled beam begins to flip the curving direction in this middle part to release the elastic energy until it meets another stable shape (S_2). By linearly interpolating these 7 images to 13 images through the same technique and using them as initial guess for NEB, we can capture the MEP more accurately by increasing the image's resolution along this pathway. As shown in Figure 4(d), the MEP with 13 images is plotted in terms of y_c and E, which is also close to the indentation through displacement control. Based on this result, the energy barrier of this symmetric transition path is 0.0193 mJ, which is higher than that of the asymmetric transition path because of the additional constraint.

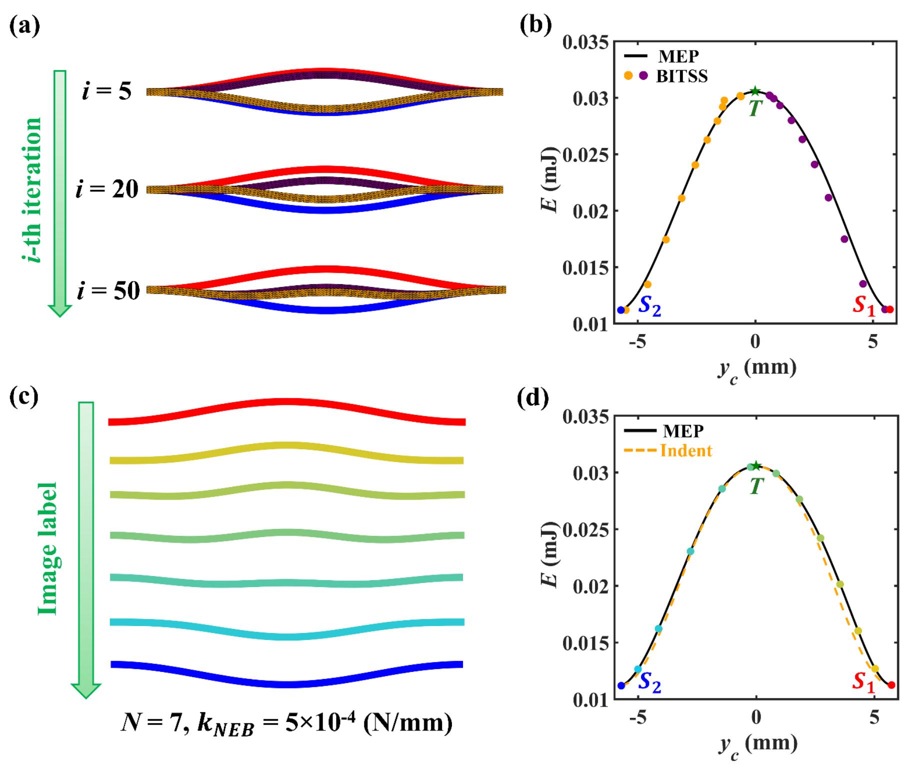

Figure 4. The symmetric transition path for a buckled beam with ε_c = 1%, $\phi_1 = \phi_2$ = 0°. (a) The shapes of the two images during iterations in the BITSS method. (b) The variation of the energy E of two images every five iterations in the BITSS method. (c) The shapes of 7 images in the NEB method with spring stiffness k_{NEB} = 5×10^{-4} N/mm. (d) The MEP based on a spline-interpolation of 13 images (circles) from the NEB results. In all figures, the red and blue color represent S_1 and S_2, respectively. The green asterisk is the saddle point by averaging the two images of the last iteration in the BITSS method. The purple and orange color denote to the two images in the BITSS method. The black curve is the MEP, and the orange dash line is the mechanical indentation.

3.2. Asymmetric Energy Landscape

The two stable states of a buckled beam can have different elastic energies if we rotate one clamped end. Here we study a representative case where the left end of the beam does not rotate ϕ_1 = 0° while the right end rotates clockwise with ϕ_1 = 5°. The compressive strain ε_c is also set as 1%. Two asymmetric stable buckling configurations can be identified, which are shown in red and blue in Figure 5(a).

The iterations of the BITSS method are shown in Figure 5(a). In this case, the mirror symmetry is lost for both stable states, and there is only one sinusoidal saddle point that exists – its mirror reflection disappears when the boundary symmetry is lost. The energy variations of two images during the iterations are shown in Figure (b) together with the MEP in terms of y_c and E. The MEP is now asymmetric with the state S_1 containing lower elastic energy and higher energy barrier while the state S_2 having higher elastic energy and lower energy barrier. Accordingly, the image that starts from S_1 has larger change between adjacent iterations compared to the other image, and two images successfully converge to the saddle point. The NEB results based on 9 images are displayed in Figure 5(c) to illustrate the shape change of the buckled beam along the MEP of this asymmetric energy landscape. Starting from the state S_1, the deflection occurs mainly near the left end when approaching the saddle point. After reaching the saddle point, the buckled beam deflects downwards near its right end to decrease the elastic energy until it becomes the other stable shape (S_2). Apart from the shape change, the energy variation of the buckled beam along the MEP is shown in Figure 5(d) based on the NEB calculation with 17 images. The stable state S_1 has elastic energy as E_{S_1} = 0.0084 mJ while the stable state S_2 has energy as E_{S_2} = 0.0144 mJ. The saddle point contains the energy as E_T = 0.0171 mJ, giving the energy barrier as 0.0087 mJ for S_1 and 0.0027 mJ for S_2.

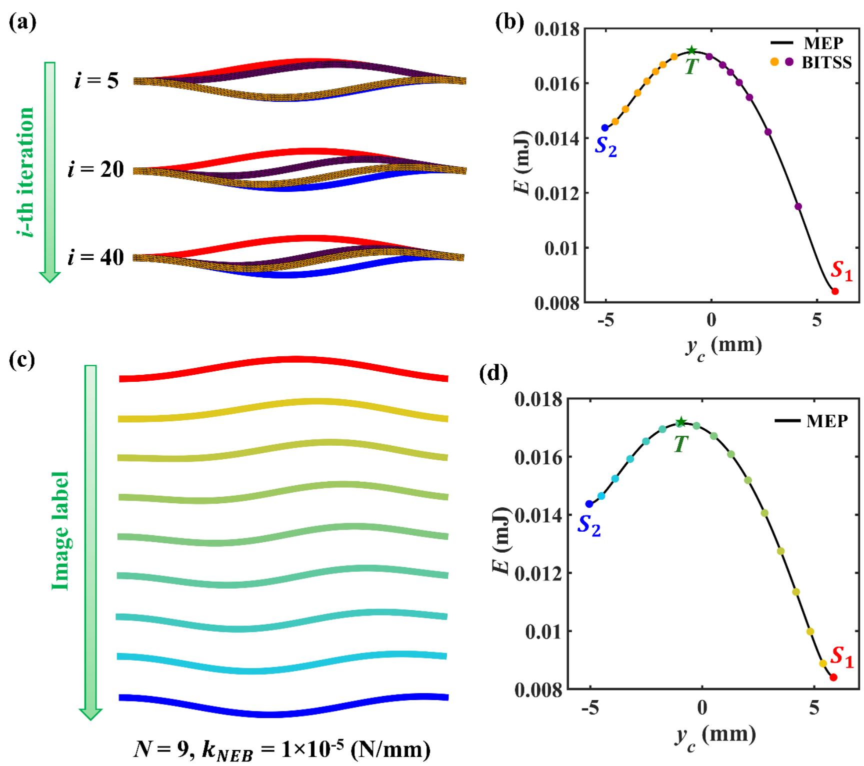

Figure 5. The transition path for a buckled beam with ε_c = 1%, ϕ_1 = 0°, ϕ_2 = 5° (a) The shapes of the two images during iterations in the BITSS method. (b) The variation of the energy E of two images every five iterations in the BITSS method. (c) The shapes of 9 images in the NEB method with spring stiffness k_{NEB} = 1×10^{-5} N/mm, different colors are assigned for images for better visualization. (d) The MEP based on a spline-interpolation of 17 images (circles) from the NEB results. In all figures, the red and blue color represent S_1 and S_2, respectively. The purple and orange color denote to the two images in the BITSS method. The green asterisk is the saddle point by averaging the two images of the last iteration in the BITSS method, and the black curve is the MEP.

We would like to point out here that, for asymmetric energy landscape where the two stable states have different energies and thus energy barriers, the parameters α and β used in the BITSS algorithm sometimes need to be adjusted so that two images can converge to the saddle point. The recommended values α = 10, β = 0.1 work well for many cases as demonstrated by the previous work (Avis et al., 2022) and all examples mentioned above. However, when the difference between energy barriers becomes significant, the image that initiates from the meta-stable state will cross over the energy barrier if these recommended values are chosen. For instance, for the same straight beam, when we axially compress it with strain ε_c = 5% and rotate its left end clockwise with θ_1 = 17° (Figure 6(a)), its two stable states have different energy as E_{S_1} = 0.0391 mJ and E_{S_2} = 0.0878 mJ. In this case, the captured saddle point through a successful implementation of the BITSS method has energy as E_T = 0.0957 mJ. In this case, the energy barriers for the states S_1 and S_2 are 0.0566 mJ and 0.0079 mJ, respectively, and the difference in energy barriers is 0.0487 mJ, which is 7 times higher than that of the previous example (0.006 mJ). As shown in Figure 6(a)-(b), the image that starts from S_2 will get over the energy barrier and converge to the stable state S_1 with the other image under the recommended values of α and β in the BITSS algorithm.

To resolve this issue, we increase the magnitude of the energy penalty term $k_e(E_1 - E_2)^2$ in the total energy in BITSS to ensure that the two images are located at different sides of the saddle point during iterations. Since the spring stiffness k_e is linearly related to the parameter α (Eq. 2.4), we choose a larger value as α = 20 instead of the recommended value. As shown in Figure 6(c)-(d), with the adjusted parameters, the two images stay at two sides of the saddle point along MEP as the BITSS algorithm proceeds and converge to the saddle point in the end, suggesting that this parameter adjustment technique can be utilized in the future if one image slides off the "ridge". It is also worth noting that, while the BITSS parameters may need some adjustments depending on the systems of interest, the method itself is robust. Typically, a reasonable range of choices for the parameter values will converge to the same result.

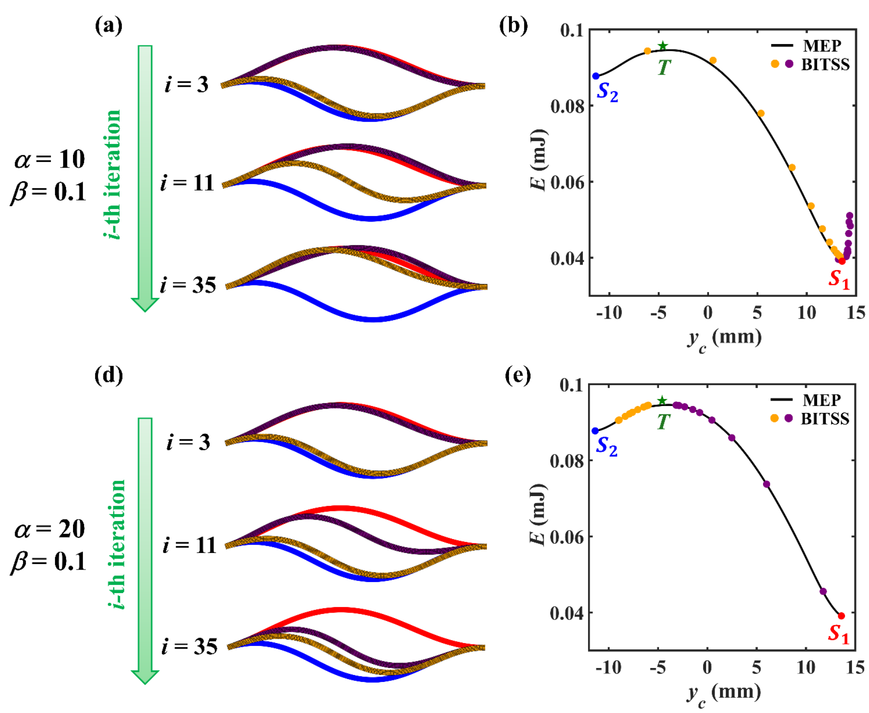

Figure 6. The transition path for a buckled beam with ε_c = 5%, ϕ_1 = 17°, ϕ_2 = 0°. The shapes and energy of the two images during iterations in the BITSS method are shown in (a) and (b) when α = 10, β = 0.1, in

(c) and (d) when $\alpha = 20$, $\beta = 0.1$, respectively. In all figures, the red and blue colors denote to S_1 and S_2 states while the purple and orange colors denote to two images in the BITSS method, respectively. The black curve is the MEP, and the green asterisk is the saddle point captured by the BITSS method.

4. Bistable Unit of Mechanical Metamaterials

In this section, we focus on another type of 2D bistable structure that features two tilted straight beams with clamped ends (Figure 7(a)). In addition to the stress-free configuration (S_1), this structure has another stable shape when two beams are compressed and sheared at one end (S_2, Figure 7(a)), which can be obtained through a vertical indentation of the structure's top edge. Such a bistable design serves as a building unit for multi-stable mechanical metamaterials that have very promising potentials in applications of impact absorption (Shan et al., 2015), logic operation (Jiang et al., 2019; Wu and Pasini, n.d.), etc., and the information of energy barrier is significant in determining the performance of metamaterials in these applications. Therefore, we employ the BITSS and NEB to seek the saddle point and MEP of this type of structure. The previous study has demonstrated that the bistable behavior depends heavily on the geometry (Shan et al., 2015), and here we investigate two situations with qualitatively different geometric features. In the first situation, the two elastic beams have the same geometric parameters including the thickness w and the tilting angle ψ. As a result, the structure contains mirror symmetry, and the two beams are under the same deformation along the MEP, similar to the indentation process in the previous report (Shan et al., 2015). In the second situation, we break the mirror symmetry by assigning two beams with the same width yet different tilting angles. This situation has a complicated energy landscape and an unintuitive transition path that will be shown later, cannot simply be reproduced through the conventional mechanical indentation.

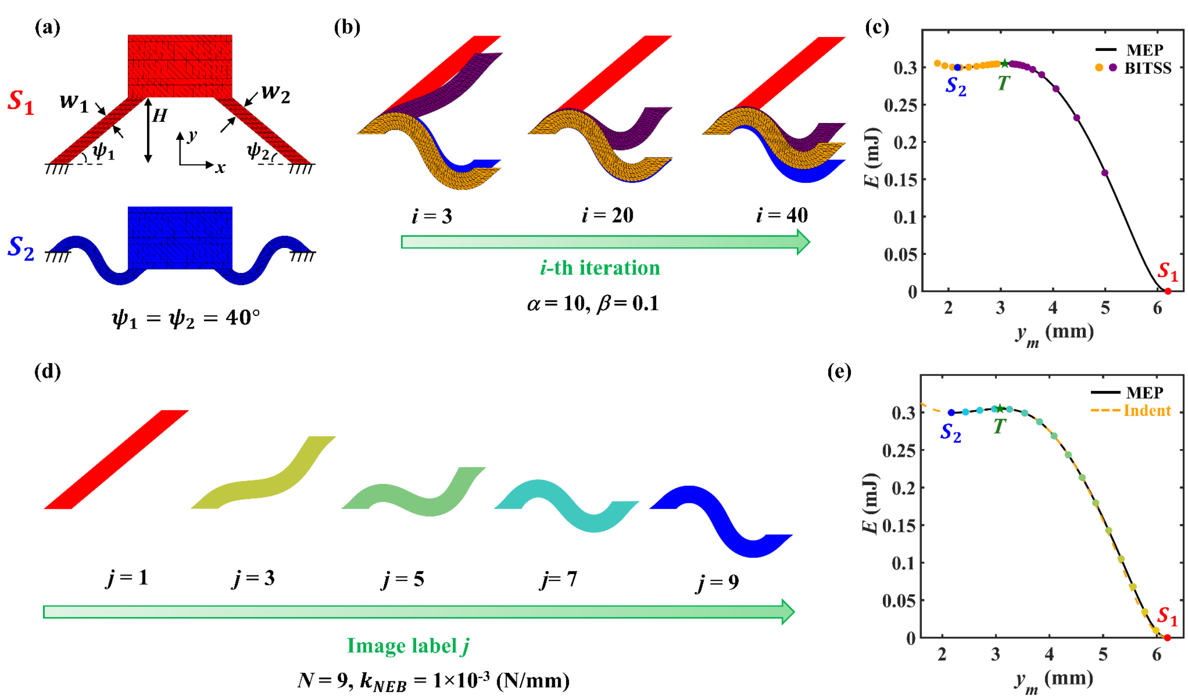

Figure 7. The symmetric transition path for a bistable unit. (a) Illustration of the geometric parameters and two stable shapes of a bistable unit with symmetric geometry (ψ_1 = 40°, ψ_2 = 40°). (b) The shapes of one tilted beam of two images during iterations of the BITSS method when α = 10 and β = 0.1. (c) The energy E of two images every three iterations in the BITSS method along with the MEP. (d) The shapes of 5 images out of 9 images in the NEB method with spring stiffness k_{NEB} = 1×10^{-3} N/mm. (e) The MEP based on a spline-interpolation of 17 images (circle) from the NEB results. In all figures, the red and blue color represent the stress-free and self-stressed shapes, respectively. The green asterisk is the saddle point by averaging the two images of the last iteration in the BITSS method. The purple and orange color denote to the two images in the BITSS method. The black curve is the MEP, and the orange dash line is the mechanical indentation.

4.1. Symmetric Transition Path

We first study the case when the two beams have the same geometry. To generate the bistable behaviors, the width w_1, w_2 and the tilting angles ψ_1, ψ_2 are chosen as w_1 = w_2 = 0.58 mm, ψ_1 = ψ_2 = 40°. The height of the beam is H = 3.2 mm. For simplicity, the two beams have the same material property as μ = 1 MPa, λ = 3 MPa. The bottom edges of the beams are clamped while the top ends are connected to a rigid block with material property μ = 38.5 MPa, λ = 57.7 MPa. The geometric domain is discretized into triangular meshes. For the beams, the mesh sizes are 0.1 mm and 0.2 mm along the length and width directions, respectively. For the top block, the size of the meshes is roughly 0.3 mm. We set up a top block that is far more rigid than the beams, ensuring that the boundary condition of the top end is close to being clamped. We build a Cartesian coordinate whose origin is located with equal distance to the centers of the beam's bottom edges. At the same time, the x axis is built along the bottom edge while the y axis is along the vertical direction.

To obtain the self-locked shape S_2, we first indent the structure at the top edge of the block to a certain distance of 5 mm and then relax this displacement boundary condition to let the structure seek its local equilibrium nearby. As shown in Figure 7(a), two stable shapes keep the mirror symmetry with the same deformation for the two tilted beams. Using the BITSS algorithm with parameters α = 10, β = 0.1, we can capture the saddle point, and the shapes of two images during iterations are shown in Figure 7(b). For clarity, we only show the deformation of one tilted beam since the mirror symmetry is kept in the BITSS iterations. As BITSS continues, the image that initiates at the stress-free shape bends significantly downwards in its middle part and undergoes larger deformation compared to that of the other image. In the meanwhile, the image that starts from the self-stress state initially bends downwards because the constraint applied in the BITSS requires it to maintain a certain distance to the top image. However, it later bends upwards and approaches the saddle point. This shape change can also be clearly seen if we plot the energy of two images during iteration together with the MEP in terms of the y coordinate of the center point of the block's bottom edge y_m. As shown in Figure 7(c), the top image (purple dots) keeps climbing uphill towards the saddle point while the bottom image (orange dots) first moves away from the saddle point and then approaches the saddle point when the top image is close.

The approximated saddle point is used to initiate the NEB method with 9 images, and the results are shown in Figure 7(d), where one tilted beam is displayed because of the mirror symmetry. Following the MEP from the stress-free shape, the beam initially develops a bending curvature downwards in its middle part as the top end moves downwards and reaches the saddle point with a sinusoidal-like configuration. After passing the saddle point, the beam relaxes itself as the top end continues to move until it becomes the self-stressed stable state. The energy variation along the MEP is shown in Figure 7(e) based on the NEB results using 17 images. The stable states have energy as E_{S_1} = 0 mJ and E_{S_2} = 0.2997 mJ while the saddle point contains elastic energy as E_T = 0.3049 mJ. Accordingly, the energy barriers for the stress-free (S_1) and self-stressed (S_2) states are 0.3049 mJ and 0.0052 mJ, respectively.

4.2. Asymmetric Transition Path

For a bistable unit with a symmetric configuration as presented in the last subsection, its saddle point and the MEP can also be obtained through indenting the top edge of the block since the structure keeps the mirror symmetry along the transition path (Figure 7(e)). The indentation can also be applied to the center of the buckled beam to obtain the saddle point, as shown in Figure 3(f) and Figure 4(d), though the indentation is slightly different from the MEP in these two cases. However, if the bistable structure has asymmetric geometry, its MEP can be complex and un-intuitive and thus cannot be captured through a simple mechanical indention. Such asymmetric configurations and transition path may offer advantages in controllable, directional force output in robots when bistable structures act as actuators (Wang et al., 2023). Therefore, it is necessary to call for a robust method instead of indentations in these situations to find the saddle point and transition path.

To demonstrate the capability of our proposed numerical method in asymmetric cases, the bistable unit is designed to have two tilted beams with different geometric parameters. Specifically, two beams have different width as w_1 = 0.58 mm, w_2 = 0.55 mm and tilting angles as ψ_1 = 40°, ψ_2 = 45°, respectively. The height H is chosen as H = 3.2 mm. The two beams have the same mesh divisions, which are 50 and 4 along the length and width directions, respectively. The mesh size of the top block is around 0.3 mm. To obtain the self-stressed equilibrium shape, we first compress the top edge of the structure downwards through displacement control and then remove this constraint to relax the structure to a stable shape nearby through static analysis. With such an initial geometry, the two beams have different deflections in the self-stress shape, forming a tilting angle φ = 3.34° between the top edge of the rigid block and the horizontal direction (Figure 8(a)). This tilting angle is determined through coordinates of two nodes on the top edge. The two stable states have their elastic energy as E_{S_1} = 0 mJ and E_{S_2} = 0.307 mJ.

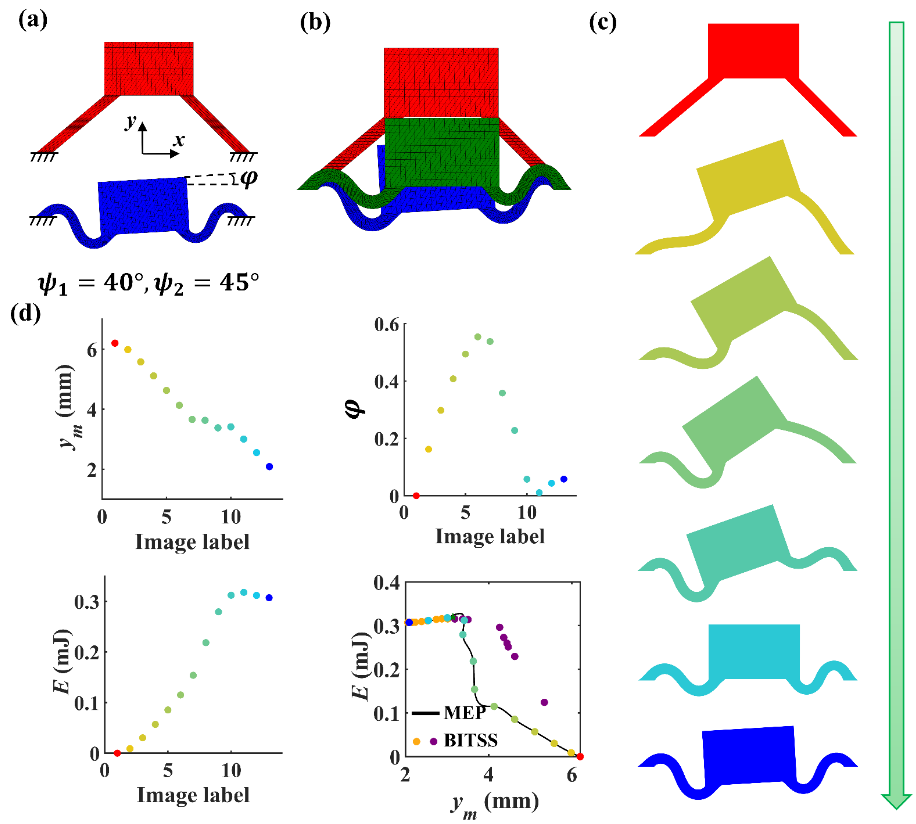

Figure 8. The asymmetric transition path for a bistable unit with ψ_1 = 40°, ψ_2 = 45°. (a) The shape of the stress-free and self-stressed shapes of the bistable unit. (b) The saddle point (green) captured by the BITSS method when α = 10, β = 0.1, f = 5%. (c) The shapes of 7 images from the NEB results with spring stiffness k_{NEB} = 4×10^{-3} N/mm. (d) The MEP (black curve) based on a spline-interpolation of 13 images from the NEB results. The purple and orange circles denote to the two images in the BITSS method. The figure includes the variation of y_m, rotational angle φ and elastic energy E along 13 images and the relationship between E and y_m along the MEP. In all figures, the red and blue colors denote to the stress-free (S_1) and self-stressed states (S_2), respectively.

We initiate the BITSS algorithm with two stable states, and the parameters are chosen as α = 10, β = 0.1, f = 5%. Unlike the previous examples, in this case, the two images during the BITSS algorithm do not follow the MEP, as shown in Figure 8(d). Averaging the two images in the last iteration, we obtain the saddle point whose configuration is closer to the self-stress state with a smaller tilting angle φ = 0.33° (Figure 8(b)). The saddle point contains elastic energy as E_T = 0.319 mJ, resulting in energy barrier as 0.319 mJ and 0.012 mJ for S_1 and S_2, respectively. Employing the NEB method with 13 images and k_{NEB} = 4×10^{-3} N/mm, we find the MEP based on the captured saddle point and reveal the shape change along this transition path in Figure 8(c). In addition, a quantitative representation of this MEP can be found in Figure 8(d) in which the elastic energy E, the y coordinate of the center of the block's bottom edge y_m and the rotating angle φ of these images are plotted versus the image's label in a sequential manner.

Following the MEP from the stress-free shape, the left beam with $\psi_1 = 40°$ first bends downwards while the right beam with $\psi_2 = 45°$ bends upwards initially. As a result, the right block moves downwards with decreasing y_m and rotates counterclockwise with increasing angle φ (Figure 8(d)). The largest rotational angle φ is 31.7°. As the left beam becomes sinusoidal, the right beam begins to bend downwards. During this stage, the rigid block starts to rotate clockwise with decreasing φ as it continues to move downwards with decreasing y_m. Unlike the non-monotonic variation of the angle φ, the elastic energy E keeps increasing before the structure meets its saddle point. After passing the saddle point, the structure decreases its elastic energy E when the rigid block again rotates counterclockwise with increasing φ to reach the self-stress shape.

The implementation of the NEB algorithm can be highly nonlinear, and a successful search for the MEP depends on good initial guess and appropriate choose of the spring stiffness k_{NEB}. In our numerical framework, we exploit the BITSS results to provide good initial guess for the NEB method to ensure good convergence. Such a treatment becomes necessary when the MEP deviates significantly from a linear interpolation between two stable states. For instance, for the asymmetric bistable unit that is studied in this section, the NEB method with 7 images requires only 77 iterations to converge to the MEP based on the BITSS results. However, using the same number of images and spring stiffness k_{NEB}, the NEB fails to converge to the MEP after 2000 iterations if a linear interpolation between two stable states is chosen as the initial guess (Figure 9). Considering that the BITSS method only requires two images to capture the saddle point, which is cheap in both storage and computational time, our numerical pipeline is more efficient than a direct implementation of the NEB algorithm that is initiated with a linear interpolation between two stable states.

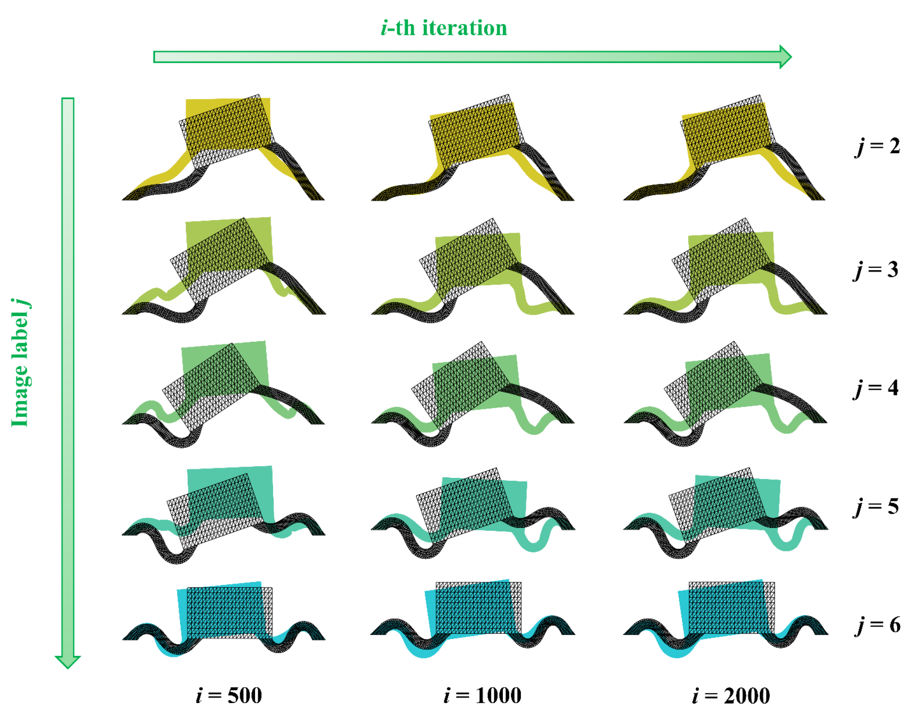

Figure 9. Comparison between the NEB results in the introduced numerical framework (unfilled shapes) and the NEB results that are initiated with a linear interpolation between two stable states (colored shapes). In both cases, the image number is 7 and the spring stiffness k_{NEB} = 4×10^{-3} N/mm.

4.3. Experimental Validation

The predicted saddle point and the MEP will not only offer the energy barrier quantitatively but also point out an efficient pathway along which a bistable structure can transition from one stable state to the other. This knowledge becomes even more valuable for bistable structures with complicated, unintuitive MEP. Here, based on the asymmetric bistable unit that is presented in the last subsection, we experimentally validate that the MEP acquired through our numerical framework can serve as useful guidance to a successful shape transition, which cannot be achieved through an intuitive uniaxial compression.

Specifically, we fabricate a bistable unit with asymmetric geometry through laser-cutting of cured polydimethylsiloxane (PDMS, SYLGARD® 184, synthesized by mixing the base and curing agent at a 10:1 weight ratio; Sigma-Aldrich) using a CO_2 laser (VLS 2.3, University Laser System, Norman, CT). The bistable PDMS structure contains two tilted beams with the following geometric parameters: w_1 = w_2 = 1 mm, ψ_1 = 45°, ψ_2 = 50°, H = 7 mm, and a uniform thickness of 3 mm. The two beams are connected by a T-block and a U-block at their top and bottom ends, respectively. For the shape transition, we place the PDMS structure horizontally on a high-density polyethylene (HDPE) substrate with negligible friction to rule out the effect of gravity. Stiff wood bars are used to push the top edge to control the deformation of the structure. Please note that we paint the top surface of the PDMS structure using a black marker to enhance the contrast for imaging purposes, and we assume that the very thin layer of paint has negligible effect on the shape transition.

In simulation, only a 2D plane strain case with the same geometry is considered for simplicity, and the material property is set as μ = 1 MPa and λ = 3 MPa. The bottom edge of the structure is clamped to avoid rigid body motion, and the geometric domain is divided into triangular meshes. The two tilted beams have the mesh divisions as 50 and 4 along their length and width directions, respectively, whereas the mesh size of the rest domain is around 0.7 mm. To obtain the self-stressed state (S_2), we uniaxially compress the top edge of the structure with 6 mm through displacement control and then remove this boundary condition to let the structure relax itself to a stable shape nearby through static analysis. In the BITSS algorithm, the parameters are chosen as α = 25, β = 0.1 and f = 5%. In the NEB method, we use 7 images, and the spring stiffness is set as k_{NEB} = 3×10^{-5} N/mm.

Both experimental and simulation results show that the structure has a self-stressed stable shape (vii in Figures 10(a) and 10(b)) in addition to the stress-free shape (i in Figures 10(a) and 10(b)). The MEP obtained in the simulation is shown in Figure 10(a). Following the MEP, the top block of the structure undergoes both linear and rotational motion as the two beams bend downwards sequentially, which is similar to the previous example. Guided by this numerical result, we first indent the right half of the top surface of the block using one stiff wood bar to rotate the top block clockwise (ii and iii in Figure 10(b)). Then we use another wood bar to push the left half of the top surface to induce counterclockwise rotation of the top block (iv-vi in Figure 10(b)), while maintaining the force exerted on the right half from the wood bar. Finally, we remove the two bars and let the structure relax to the self-stressed state (vii in Figure 10(b) and supplementary Video 1). However, if we employ an intuitive strategy by directly compressing the top surface without rotating the top block, the structure will bounce back to the initial stress-free state once the bar is withdrawn (Figure 10(c) and supplementary Video 2). We run additional experiments to verify that the reconfiguration process is robust, and the self-stressed state is stable even after 25 s relaxation (supplementary Video 3). Such a failure to complete the shape transition is observed under various compression depth and speed, which is also supported by finite element simulation in commercial software ABAQUS based on dynamic analysis (top row in Figure 11). The reason can be attributed to the fact that the pure compression cannot help the structure reach the self-stressed stable shape due to the non-equilibrium stress even the structure has crossed the "ridge" and get close to the local minimum in the energy landscape. With this specific geometry, the structure has energy as 0.794 mJ at the meta-stable state (S_2). The energy of the transition state is 0.838 mJ, leading to the energy barrier as 0.044 mJ. While the structure compressed at 12 mm has an energy of 0.847 mJ, whose energy difference from S_2 (0.053 mJ) is higher than the energy barrier. As a result, once the external constraint is lifted, the extra elastic energy compared to the meta-stable state (S_2) will convert to kinetic energy and drive the structure to cross over the small energy barrier and move to the stress-free state (S_1) with a lower elastic energy and higher energy barrier (0.794 mJ). To test the kinetic effect in the shape transition, we further run a static simulation using ABAQUS and find the structure will converge to S_2 (bottom row in Figure 11). The energy barrier of the bistable metamaterials is known to depend on geometries of the structures (Shan et al., 2015). Thus, it is of great interests in exploring the geometrical parameter space to optimize energy barrier for easy and robust reconfigurations, which will be conducted in future studies.

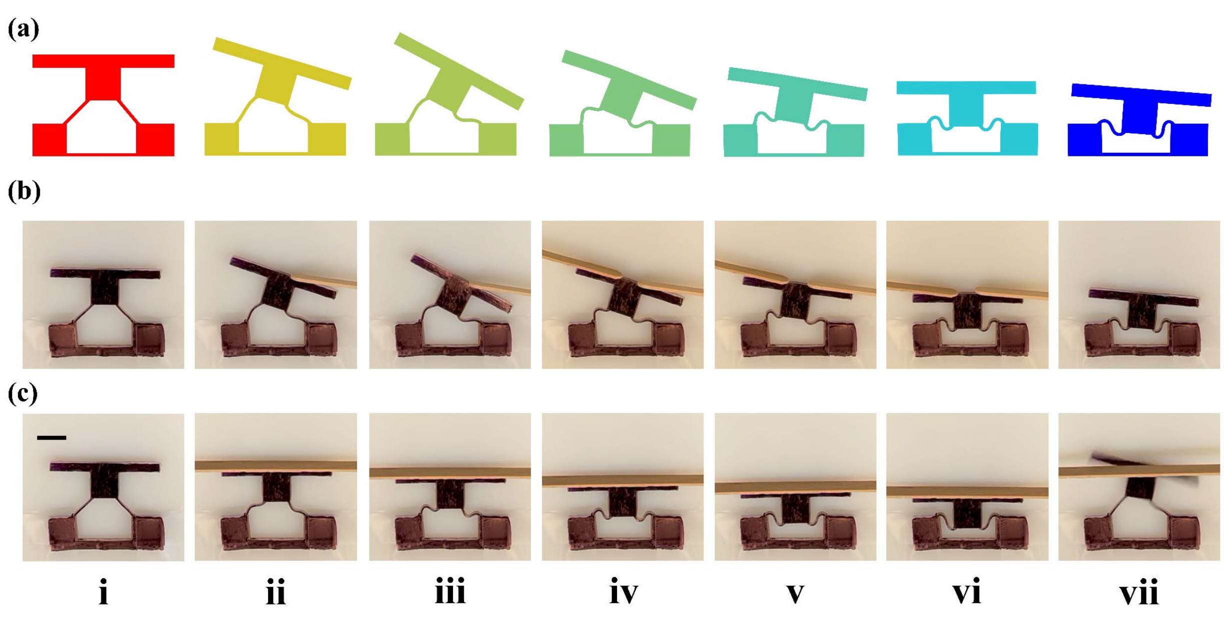

Figure 10. Experimental validation of the MEP from the proposed numerical framework. (a) The shapes of 7 images along the MEP. The red and blue colors denote the stress-free and self-stressed states, respectively. (b) The successful shape transition in the experiment following the MEP. (c) Under a pure compression in experiment, the bistable unit bounces back to the stress-free shape once the constraint is removed. The scale bar is 10 mm.

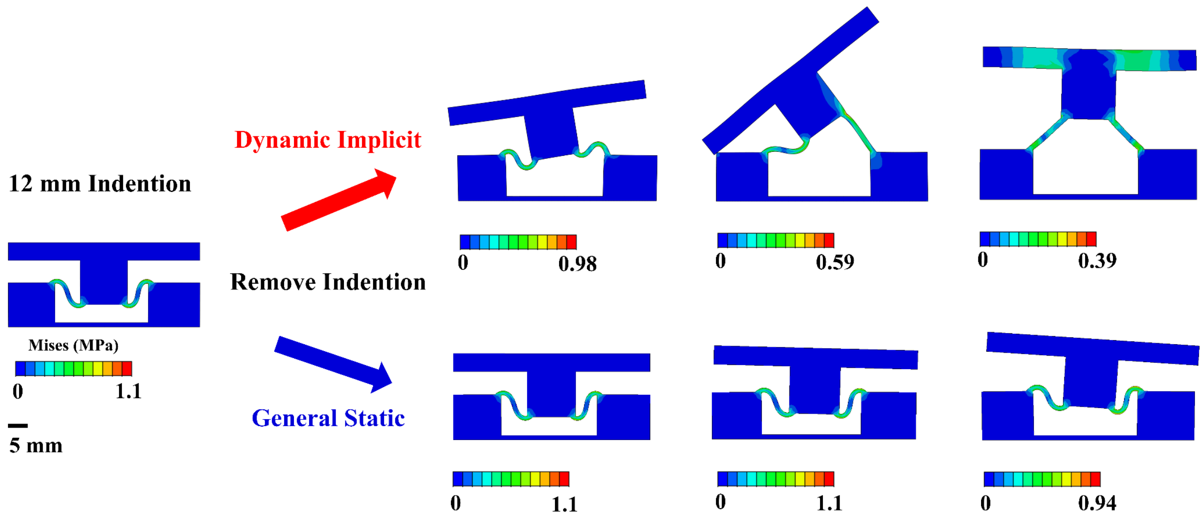

Figure 11. Comparison between the dynamic and static simulations. After removal of 12 mm indentation, the bistable unit can snap back to S_1 under dynamic analysis (top row) or converge to S_2 nearby under general static analysis (bottom row). The scale bar is 5 mm.

5. Conclusion

In this work, we introduce a robust computational framework by integrating the BITSS and NEB algorithms into FEM to find the saddle point and the associated MEP of bistable elastic continua. In this numerical pipeline, the BITSS algorithm that manipulates two images is first employed to pinpoint the saddle point. Then we use gradient descent algorithm based on the captured saddle point to initiate the NEB method that relaxes a string of images to converge to the MEP. We successfully verify the performance of the proposed framework in two representative cases including bistable buckled beams and bistable units from mechanical metamaterials, under both symmetric and asymmetric conditions. The obtained saddle point and MEP can not only provide the information of the energy barrier, which offers quantitative evaluation of the performance of bistable structures, but also point out an efficient transition pathway that guides the shape transition of bistable structures either under either mechanical force in this work or distributed body force through external stimuli such as magnetic field.

The proposed numerical framework has its advantages in several aspects. First, it is built on FEM that is widely adopted to model the mechanical behaviors of solids, suggesting that the proposed method can be broadly applied in analyzing the energy landscape of multi-stable structures. Second, previous work has demonstrated that the combination of the BITSS and string method can capture the MEP and saddle point of multi-stable slender structures based on a discrete shell model (Y. Li et al., 2021a). Since the string method is an efficient double-ended method that converges to the MEP through relaxing a string of images, its similarity to the NEB suggests that our method has great potentials in searching for multiple saddle points and MEPs in multi-stable elastic continua. Third, because the BITSS method requires only two images to find the saddle point, its implementation together with the NEB algorithm can be more computation-efficient in find the MEP than directly applying the NEB that is initiated with a linear interpolation between two stable states, particularly for systems with large number of DoF.

Only 2D plane strain problems under displacement boundary conditions are considered in this study. However, the introduced numerical framework should be seamlessly integrated into 3D finite element modeling under various types of boundary conditions such as concentrated or distributed force, greatly expanding the range of application of our methods. In addition, by integrating potential energies associated with other fields, our method should also be capable of solving multi-physics problems where the bistable structures are subjected to external stimuli such as magnetic fields (Y. Li et al., 2021a, 2021b) or differential swelling (Li et al., 2023). Such a characteristic enables the search for the energy barrier and transition path of bistable structures made of stimuli-responsive materials, which can facilitate their applications in controllable shape change (Ma et al., 2023; Shao et al., 2018; Zhao et al., 2016), fast actuation (Wani et al., 2017), etc.

Acknowledgement

G. Wan and T. Zhang would like to thank the support from the National Science Foundation (NSF) (Grant No. CMMI 2103012). Z.Z. Wang and X.J. Wang would like to acknowledge the support from the NSF (Grant No. CMMI 2103012). S.J. Avis is supported by a studentship from the Engineering and Physical Sciences Research Council (Grant No. EP/R513039/1). H. Kusumaatmaja acknowledges funding from the Engineering and Physical Sciences Research Council (Grant No. EP/V034154/1). Simulations were performed at the Expanse cluster (Award no. TG-MSS170004) in the Advanced Cyberinfrastructure Coordination Ecosystem: Services & Support (ACCESS).

Declaration of generative AI and AI-assisted technologies in the writing process

During the preparation of this work the authors used ChatGPT in order to correct grammar and refine the language. After using this tool/service, the author reviewed and edited the content as needed and take full responsibility for the content of the publication.

References

Abbasi, A., Sano, T.G., Yan, D., Reis, P.M., 2023. Snap buckling of bistable beams under combined mechanical and magnetic loading. Philosophical Transactions of the Royal Society A:

Mathematical, Physical and Engineering Sciences 381, 20220029. https://doi.org/10.1098/rsta.2022.0029

Arrieta, A.F., Delpero, T., Bergamini, A.E., Ermanni, P., 2013. Broadband vibration energy harvesting based on cantilevered piezoelectric bi-stable composites. Appl. Phys. Lett. 102, 173904. https://doi.org/10.1063/1.4803918

Arrieta, A.F., Hagedorn, P., Erturk, A., Inman, D.J., 2010. A piezoelectric bistable plate for nonlinear broadband energy harvesting. Appl. Phys. Lett. 97, 104102. https://doi.org/10.1063/1.3487780

Arrieta, A.F., Kuder, I.K., Rist, M., Waeber, T., Ermanni, P., 2014. Passive load alleviation aerofoil concept with variable stiffness multi-stable composites. Composite Structures 116, 235–242. https://doi.org/10.1016/j.compstruct.2014.05.016

Ásgeirsson, V., Birgisson, B.O., Bjornsson, R., Becker, U., Neese, F., Riplinger, C., Jónsson, H., 2021. Nudged Elastic Band Method for Molecular Reactions Using Energy-Weighted Springs Combined with Eigenvector Following. J. Chem. Theory Comput. 17, 4929–4945. https://doi.org/10.1021/acs.jctc.1c00462

Avis, S.J., Panter, J.R., Kusumaatmaja, H., 2022. A robust and memory-efficient transition state search method for complex energy landscapes. The Journal of Chemical Physics 157, 124107. https://doi.org/10.1063/5.0102145

Bohner, M.U., Zeman, J., Smiatek, J., Arnold, A., Kästner, J., 2014. Nudged-elastic band used to find reaction coordinates based on the free energy. The Journal of Chemical Physics 140, 074109. https://doi.org/10.1063/1.4865220

Bolhuis, P.G., Chandler, D., Dellago, C., Geissler, P.L., 2002. TRANSITION PATH SAMPLING: Throwing Ropes Over Rough Mountain Passes, in the Dark. Annual Review of Physical Chemistry 53, 291–318. https://doi.org/10.1146/annurev.physchem.53.082301.113146

Boston, D.M., Phillips, F.R., Henry, T.C., Arrieta, A.F., 2022. Spanwise wing morphing using multistable cellular metastructures. Extreme Mechanics Letters 53, 101706. https://doi.org/10.1016/j.eml.2022.101706

Champneys, A.R., Dodwell, T.J., Groh, R.M.J., Hunt, G.W., Neville, R.M., Pirrera, A., Sakhaei, A.H., Schenk, M., Wadee, M.A., 2019. Happy Catastrophe: Recent Progress in Analysis and Exploitation of Elastic Instability. Frontiers in Applied Mathematics and Statistics 5.

Chen, D., Costello, L.L., Geller, C.B., Zhu, T., McDowell, D.L., 2019. Atomistic modeling of dislocation cross-slip in nickel using free-end nudged elastic band method. Acta Materialia 168, 436–447. https://doi.org/10.1016/j.actamat.2019.02.035

Chen, T., Mueller, J., Shea, K., 2017. Integrated Design and Simulation of Tunable, Multi-State Structures Fabricated Monolithically with Multi-Material 3D Printing. Sci Rep 7, 45671. https://doi.org/10.1038/srep45671

Chi, Y., Hong, Y., Zhao, Y., Li, Y., Yin, J., 2022. Snapping for high-speed and high-efficient butterfly stroke–like soft swimmer. Science Advances 8, eadd3788. https://doi.org/10.1126/sciadv.add3788

Crisfield, M.A., 1981. A fast incremental/iterative solution procedure that handles “snap-through.” Computers & Structures 13, 55–62. https://doi.org/10.1016/0045-7949(81)90108-5

Dai, J., Lu, L., Leanza, S., Hutchinson, J., Zhao, R.R., 2023. Curved Ring Origami: Bistable Elastic Folding for Magic Pattern Reconfigurations. Journal of Applied Mechanics 1–27. https://doi.org/10.1115/1.4062221

Daynes, S., Potter, K.D., Weaver, P.M., 2008. Bistable prestressed buckled laminates. Composites Science and Technology 68, 3431–3437. https://doi.org/10.1016/j.compscitech.2008.09.036

Deng, B., Wang, P., Tournat, V., Bertoldi, K., 2020. Nonlinear transition waves in free-standing bistable chains. Journal of the Mechanics and Physics of Solids, The Davide Bigoni 60th Anniversary Issue 136, 103661. https://doi.org/10.1016/j.jmps.2019.07.004

Diaconu, C.G., Weaver, P.M., Mattioni, F., 2008. Concepts for morphing airfoil sections using bi-stable laminated composite structures. Thin-Walled Structures 46, 689–701. https://doi.org/10.1016/j.tws.2007.11.002
Eriksson, A., 1998. Structural instability analyses based on generalised path-following. Computer Methods in Applied Mechanics and Engineering 156, 45–74. https://doi.org/10.1016/S0045-7825(97)00200-4
Faber, J.A., Arrieta, A.F., Studart, A.R., 2018. Bioinspired spring origami. Science 359, 1386–1391. https://doi.org/10.1126/science.aap7753
Fang, H., Wang, K.W., Li, S., 2017. Asymmetric energy barrier and mechanical diode effect from folding multi-stable stacked-origami. Extreme Mechanics Letters 17, 7–15. https://doi.org/10.1016/j.eml.2017.09.008
Forterre, Y., Skotheim, J.M., Dumais, J., Mahadevan, L., 2005. How the Venus flytrap snaps. Nature 433, 421–425. https://doi.org/10.1038/nature03185
Fu, H., Nan, K., Bai, W., Huang, W., Bai, K., Lu, L., Zhou, C., Liu, Yunpeng, Liu, F., Wang, J., Han, M., Yan, Z., Luan, H., Zhang, Yijie, Zhang, Yutong, Zhao, J., Cheng, X., Li, M., Lee, J.W., Liu, Yuan, Fang, D., Li, X., Huang, Y., Zhang, Yihui, Rogers, J.A., 2018. Morphable 3D mesostructures and microelectronic devices by multistable buckling mechanics. Nature Materials 17, 268–276. https://doi.org/10.1038/s41563-017-0011-3
Garrido Torres, J.A., Jennings, P.C., Hansen, M.H., Boes, J.R., Bligaard, T., 2019. Low-Scaling Algorithm for Nudged Elastic Band Calculations Using a Surrogate Machine Learning Model. Phys. Rev. Lett. 122, 156001. https://doi.org/10.1103/PhysRevLett.122.156001
Ghasemi, A., Gao, W., 2020. A method to predict energy barriers in stress modulated solid–solid phase transitions. Journal of the Mechanics and Physics of Solids 137, 103857. https://doi.org/10.1016/j.jmps.2019.103857
Ghasemi, A., Xiao, P., Gao, W., 2019. Nudged elastic band method for solid-solid transition under finite deformation. The Journal of Chemical Physics 151, 054110. https://doi.org/10.1063/1.5113716
Ghavidelnia, N., Yin, K., Cao, B., Eberl, C., 2023. Curly beam with programmable bistability. Materials & Design 230, 111988. https://doi.org/10.1016/j.matdes.2023.111988
Gomez, M., Moulton, D.E., Vella, D., 2017a. Passive Control of Viscous Flow via Elastic Snap-Through. Physical Review Letters 119. https://doi.org/10.1103/PhysRevLett.119.144502
Gomez, M., Moulton, D.E., Vella, D., 2017b. Critical slowing down in purely elastic 'snap-through' instabilities. Nature Physics 13, 142–145. https://doi.org/10.1038/nphys3915
Gorissen, B., Melancon, D., Vasios, N., Torbati, M., Bertoldi, K., 2020. Inflatable soft jumper inspired by shell snapping. Sci. Robot. 5, eabb1967. https://doi.org/10.1126/scirobotics.abb1967
Groh, R.M.J., Avitabile, D., Pirrera, A., 2018. Generalised path-following for well-behaved nonlinear structures. Computer Methods in Applied Mechanics and Engineering 331, 394–426. https://doi.org/10.1016/j.cma.2017.12.001
Harne, R.L., Wang, K.W., 2013. A review of the recent research on vibration energy harvesting via bistable systems. Smart Mater. Struct. 22, 023001. https://doi.org/10.1088/0964-1726/22/2/023001
Harvey, P.S., Virgin, L.N., 2015. Coexisting equilibria and stability of a shallow arch: Unilateral displacement-control experiments and theory. International Journal of Solids and Structures 54, 1–11. https://doi.org/10.1016/j.ijsolstr.2014.11.016
Henkelman, G., Jónsson, H., 2000. Improved tangent estimate in the nudged elastic band method for finding minimum energy paths and saddle points. The Journal of Chemical Physics 113, 9978–9985. https://doi.org/10.1063/1.1323224

Henkelman, G., Uberuaga, B.P., Jónsson, H., 2000. A climbing image nudged elastic band method for finding saddle points and minimum energy paths. The Journal of Chemical Physics 113, 9901–9904. https://doi.org/10.1063/1.1329672

Holmes, D.P., Crosby, A.J., 2007. Snapping Surfaces. Adv. Mater. 19, 3589–3593. https://doi.org/10.1002/adma.200700584

Horák, J., Lord, G.J., Peletier, M.A., 2006. Cylinder Buckling: The Mountain Pass as an Organizing Center. SIAM J. Appl. Math. 66, 1793–1824. https://doi.org/10.1137/050635778

Hou, X., Liu, Y., Wan, G., Xu, Z., Wen, C., Yu, H., Zhang, J.X.J., Li, J., Chen, Z., 2018. Magneto-sensitive bistable soft actuators: Experiments, simulations, and applications. Applied Physics Letters 113, 221902. https://doi.org/10.1063/1.5062490

Huang, W., Qin, L., Chen, Q., 2022. Numerical Exploration on Snap Buckling of a Pre-Stressed Hemispherical Gridshell. Journal of Applied Mechanics 89, 011005. https://doi.org/10.1115/1.4052289

Huang, W., Zhang, Y., Yu, T., Liu, M., 2023. Bifurcations and Stability Analysis of Elastic Slender Structures Using Static Discrete Elastic Rods Method. Journal of Applied Mechanics 90, 094501. https://doi.org/10.1115/1.4062533

Jiang, Y., Korpas, L.M., Raney, J.R., 2019. Bifurcation-based embodied logic and autonomous actuation. Nat Commun 10, 128. https://doi.org/10.1038/s41467-018-08055-3

Jin, L., Khajehtourian, R., Mueller, J., Rafsanjani, A., Tournat, V., Bertoldi, K., Kochmann, D.M., 2020. Guided transition waves in multistable mechanical metamaterials. Proc Natl Acad Sci USA 117, 2319–2325. https://doi.org/10.1073/pnas.1913228117

Kolsbjerg, E.L., Groves, M.N., Hammer, B., 2016. An automated nudged elastic band method. The Journal of Chemical Physics 145, 094107. https://doi.org/10.1063/1.4961868

Li, C., Luo, H., Song, J., 2021. Magnetically Driven Non-Contact Transfer Printing Based on a Bi-Stable Elastomeric Stamp. Advanced Materials Technologies 6, 2100335. https://doi.org/10.1002/admt.202100335

Li, C.Y., Jiao, D., Hao, X.P., Hong, W., Zheng, Q., Wu, Z.L., 2023. Bistable Joints Enable the Morphing of Hydrogel Sheets with Multistable Configurations. Advanced Materials 35, 2211802. https://doi.org/10.1002/adma.202211802

Li, H., Dai, F., Du, S., 2015. Broadband energy harvesting by exploiting nonlinear oscillations around the second vibration mode of a rectangular piezoelectric bistable laminate. Smart Mater. Struct. 24, 045024. https://doi.org/10.1088/0964-1726/24/4/045024

Li, Y., Avis, S.J., Chen, J., Wu, G., Zhang, T., Kusumaatmaja, H., Wang, X., 2021a. Reconfiguration of multistable 3D ferromagnetic mesostructures guided by energy landscape surveys. Extreme Mechanics Letters 48, 101428. https://doi.org/10.1016/j.eml.2021.101428

Li, Y., J. Avis, S., Zhang, T., Kusumaatmaja, H., Wang, X., 2021b. Tailoring the multistability of origami-inspired, buckled magnetic structures via compression and creasing. Materials Horizons 8, 3324–3333. https://doi.org/10.1039/D1MH01152A

Li, Y., Pellegrino, S., 2020. A Theory for the Design of Multi-Stable Morphing Structures. Journal of the Mechanics and Physics of Solids, The Davide Bigoni 60th Anniversary Issue 136, 103772. https://doi.org/10.1016/j.jmps.2019.103772

Liu, K., Tachi, T., Paulino, G.H., 2019. Invariant and smooth limit of discrete geometry folded from bistable origami leading to multistable metasurfaces. Nat Commun 10, 4238. https://doi.org/10.1038/s41467-019-11935-x

Liu, M., Gomez, M., Vella, D., 2021. Delayed bifurcation in elastic snap-through instabilities. Journal of the Mechanics and Physics of Solids 151, 104386. https://doi.org/10.1016/j.jmps.2021.104386

Liu, W.Q., Badel, A., Formosa, F., Wu, Y.P., Agbossou, A., 2013. Novel piezoelectric bistable oscillator architecture for wideband vibration energy harvesting. Smart Mater. Struct. 22, 035013. https://doi.org/10.1088/0964-1726/22/3/035013

Liu, Y., Liang, S., Huang, Q., Hu, H., Zheng, Y., Zhang, H., Shao, Q., 2017. A robust Riks-like path following method for strain-actuated snap-through phenomena in soft solids. Computer Methods in Applied Mechanics and Engineering 323, 416–438. https://doi.org/10.1016/j.cma.2017.05.010

Liu, Y., Zeng, W., Wan, G., Dong, L., Xu, Z., Zhang, J.X.J., Chen, Z., 2019. Voltage-actuated snap-through in bistable piezoelectric thin films: a computational study. Smart Mater. Struct. 28, 085021. https://doi.org/10.1088/1361-665X/aae8be

Lu, L., Dai, J., Leanza, S., Hutchinson, J.W., Zhao, R.R., 2023a. Multiple equilibrium states of a curved-sided hexagram: Part II—Transitions between states. Journal of the Mechanics and Physics of Solids 180, 105407. https://doi.org/10.1016/j.jmps.2023.105407

Lu, L., Dai, J., Leanza, S., Zhao, R.R., Hutchinson, J.W., 2023b. Multiple equilibrium states of a curved-sided hexagram: Part I—stability of states. Journal of the Mechanics and Physics of Solids 180, 105406. https://doi.org/10.1016/j.jmps.2023.105406

Lu, L., Leanza, S., Dai, J., Sun, X., Zhao, R.R., 2023c. Easy snap-folding of hexagonal ring origami by geometric modifications. Journal of the Mechanics and Physics of Solids 171, 105142. https://doi.org/10.1016/j.jmps.2022.105142

Ma, R., Wu, L., Pasini, D., 2023. Contact-Driven Snapping in Thermally Actuated Metamaterials for Fully Reversible Functionality. Advanced Functional Materials 33, 2213371. https://doi.org/10.1002/adfm.202213371

Marthelot, J., López Jiménez, F., Lee, A., Hutchinson, J.W., Reis, P.M., 2017. Buckling of a Pressurized Hemispherical Shell Subjected to a Probing Force. Journal of Applied Mechanics 84. https://doi.org/10.1115/1.4038063

Mattioni, F., Weaver, P.M., Potter, K.D., Friswell, M.I., 2008. The application of thermally induced multistable composites to morphing aircraft structures, in: Davis, L.P., Henderson, B.K., McMickell, M.B. (Eds.), . Presented at the The 15th International Symposium on: Smart Structures and Materials & Nondestructive Evaluation and Health Monitoring, San Diego, California, p. 693012. https://doi.org/10.1117/12.776226

Meaud, J., Che, K., 2017. Tuning elastic wave propagation in multistable architected materials. International Journal of Solids and Structures 122–123, 69–80. https://doi.org/10.1016/j.ijsolstr.2017.05.042

Melancon, D., Gorissen, B., García-Mora, C.J., Hoberman, C., Bertoldi, K., 2021. Multistable inflatable origami structures at the metre scale. Nature 592, 545–550. https://doi.org/10.1038/s41586-021-03407-4

Meng, Z., Chen, W., Mei, T., Lai, Y., Li, Y., Chen, C.Q., 2021. Bistability-based foldable origami mechanical logic gates. Extreme Mechanics Letters 43, 101180. https://doi.org/10.1016/j.eml.2021.101180

Neville, R.M., Groh, R.M.J., Pirrera, A., Schenk, M., 2020. Beyond the fold: experimentally traversing limit points in nonlinear structures. Proceedings of the Royal Society A: Mathematical, Physical and Engineering Sciences 476, 20190576. https://doi.org/10.1098/rspa.2019.0576

Neville, R.M., Groh, R.M.J., Pirrera, A., Schenk, M., 2018. Shape Control for Experimental Continuation. Phys. Rev. Lett. 120, 254101. https://doi.org/10.1103/PhysRevLett.120.254101

Pal, A., Sitti, M., 2023. Programmable mechanical devices through magnetically tunable bistable elements. Proceedings of the National Academy of Sciences 120, e2212489120. https://doi.org/10.1073/pnas.2212489120

Pan, D., 2017. Experimental investigation of broadband energy harvesting of a bi-stable composite piezoelectric plate. Smart Mater. Struct. 15.

Pandey, A., Moulton, D.E., Vella, D., Holmes, D.P., 2014. Dynamics of snapping beams and jumping poppers. EPL (Europhysics Letters) 105, 24001. https://doi.org/10.1209/0295-5075/105/24001
Panter, J.R., Chen, J., Zhang, T., Kusumaatmaja, H., 2019. Harnessing energy landscape exploration to control the buckling of cylindrical shells. Commun Phys 2, 1–9. https://doi.org/10.1038/s42005-019-0251-4
Power, M., Barbot, A., Seichepine, F., Yang, G.-Z., 2023. Bistable, Pneumatically Actuated Microgripper Fabricated Using Two-Photon Polymerization and Oxygen Plasma Etching. Advanced Intelligent Systems 5, 2200121. https://doi.org/10.1002/aisy.202200121
Preston, D.J., Jiang, H.J., Sanchez, V., Rothemund, P., Rawson, J., Nemitz, M.P., Lee, W.-K., Suo, Z., Walsh, C.J., Whitesides, G.M., 2019. A soft ring oscillator. Sci. Robot. 4, eaaw5496. https://doi.org/10.1126/scirobotics.aaw5496
Qiao, C., Liu, L., Pasini, D., 2021. Bi-Shell Valve for Fast Actuation of Soft Pneumatic Actuators via Shell Snapping Interaction. Advanced Science 8, 2100445. https://doi.org/10.1002/advs.202100445
Radisson, B., Kanso, E., 2023. Elastic Snap-Through Instabilities Are Governed by Geometric Symmetries. Phys. Rev. Lett. 130, 236102. https://doi.org/10.1103/PhysRevLett.130.236102
Rao, S.I., Dimiduk, D.M., Parthasarathy, T.A., El-Awady, J., Woodward, C., Uchic, M.D., 2011. Calculations of intersection cross-slip activation energies in fcc metals using nudged elastic band method. Acta Materialia 59, 7135–7144. https://doi.org/10.1016/j.actamat.2011.08.029
Restrepo, D., Mankame, N.D., Zavattieri, P.D., 2015. Phase transforming cellular materials. Extreme Mechanics Letters 4, 52–60. https://doi.org/10.1016/j.eml.2015.08.001
Riks, E., 1979. An incremental approach to the solution of snapping and buckling problems. International Journal of Solids and Structures 15, 529–551. https://doi.org/10.1016/0020-7683(79)90081-7
Rivas-Padilla, J.R., Boston, D.M., Boddapati, K., Arrieta, A.F., 2023. Aero-structural optimization and actuation analysis of a morphing wing section with embedded selectively stiff bistable elements. Journal of Composite Materials 57, 737–757. https://doi.org/10.1177/00219983231155163
Rothemund, P., Ainla, A., Belding, L., Preston, D.J., Kurihara, S., Suo, Z., Whitesides, G.M., 2018. A soft, bistable valve for autonomous control of soft actuators. Sci. Robot. 3, eaar7986. https://doi.org/10.1126/scirobotics.aar7986
Sano, T.G., Wada, H., 2018. Snap-buckling in asymmetrically constrained elastic strips. Physical Review E 97. https://doi.org/10.1103/PhysRevE.97.013002
Sano, T.G., Yamaguchi, T., Wada, H., 2017. Slip Morphology of Elastic Strips on Frictional Rigid Substrates. Phys. Rev. Lett. 118, 178001. https://doi.org/10.1103/PhysRevLett.118.178001
Schioler, T., Pellegrino, S., 2007. Space Frames with Multiple Stable Configurations. AIAA Journal 45, 1740–1747. https://doi.org/10.2514/1.16825
Shan, S., Kang, S.H., Raney, J.R., Wang, P., Fang, L., Candido, F., Lewis, J.A., Bertoldi, K., 2015. Multistable Architected Materials for Trapping Elastic Strain Energy. Advanced Materials 27, 4296–4301. https://doi.org/10.1002/adma.201501708
Shao, H., Wei, S., Jiang, X., Holmes, D.P., Ghosh, T.K., 2018. Bioinspired Electrically Activated Soft Bistable Actuators. Advanced Functional Materials 28, 1802999. https://doi.org/10.1002/adfm.201802999
Sheppard, D., Xiao, P., Chemelewski, W., Johnson, D.D., Henkelman, G., 2012. A generalized solid-state nudged elastic band method. The Journal of Chemical Physics 136, 074103. https://doi.org/10.1063/1.3684549
Si, Y., Zhang, Y., Chen, D., Wormald, J.L., Anglin, B.S., McDowell, D.L., Zhu, T., 2023. Atomistic determination of Peierls barriers of dislocation glide in nickel. Journal of the Mechanics and Physics of Solids 105359. https://doi.org/10.1016/j.jmps.2023.105359

Silverberg, J.L., Na, J.-H., Evans, A.A., Liu, B., Hull, T.C., Santangelo, C.D., Lang, R.J., Hayward, R.C., Cohen, I., 2015. Origami structures with a critical transition to bistability arising from hidden degrees of freedom. Nature Materials 14, 389–393. https://doi.org/10.1038/nmat4232

Sobie, C., Capolungo, L., McDowell, D.L., Martinez, E., 2017. Scale transition using dislocation dynamics and the nudged elastic band method. Journal of the Mechanics and Physics of Solids 105, 161–178. https://doi.org/10.1016/j.jmps.2017.05.004

Song, K., Scarpa, F., Schenk, M., n.d. Identifying the Energy Threshold for Multistable Tensegrity Structures using a Mountain Pass Algorithm.

Taffetani, M., Jiang, X., Holmes, D.P., Vella, D., 2018. Static bistability of spherical caps. Proceedings of the Royal Society A: Mathematical, Physical and Engineering Science 474, 20170910. https://doi.org/10.1098/rspa.2017.0910

Tang, Y., Chi, Y., Sun, J., Huang, T.-H., Maghsoudi, O.H., Spence, A., Zhao, J., Su, H., Yin, J., 2020. Leveraging elastic instabilities for amplified performance: Spine-inspired high-speed and high-force soft robots. Sci. Adv. 6, eaaz6912. https://doi.org/10.1126/sciadv.aaz6912

Thompson, J.M.T., Hutchinson, J.W., Sieber, J., 2017. Probing Shells Against Buckling: A Nondestructive Technique for Laboratory Testing. Int. J. Bifurcation Chaos 27, 1730048. https://doi.org/10.1142/S0218127417300488

Tian, Z., Xu, B., Wan, G., Han, X., Di, Z., Chen, Z., Mei, Y., 2021. Gaussian-preserved, non-volatile shape morphing in three-dimensional microstructures for dual-functional electronic devices. Nat Commun 12, 509. https://doi.org/10.1038/s41467-020-20843-4

Trygubenko, S.A., Wales, D.J., 2004. A doubly nudged elastic band method for finding transition states. The Journal of Chemical Physics 120, 2082–2094. https://doi.org/10.1063/1.1636455

Vasios, N., Deng, B., Gorissen, B., Bertoldi, K., 2021. Universally bistable shells with nonzero Gaussian curvature for two-way transition waves. Nat Commun 12, 695. https://doi.org/10.1038/s41467-020-20698-9

Virot, E., Kreilos, T., Schneider, T.M., Rubinstein, S.M., 2017. Stability Landscape of Shell Buckling. Phys. Rev. Lett. 119, 224101. https://doi.org/10.1103/PhysRevLett.119.224101

Wales, D., 2004. Energy Landscapes: Applications to Clusters, Biomolecules and Glasses. Cambridge University Press.

Wan, G., Cai, Y., Liu, Y., Jin, C., Wang, D., Huang, S., Hu, N., Zhang, J.X.J., Chen, Z., 2021. Bistability in popper-like shells programmed by geometric defects. Extreme Mechanics Letters 42, 101065. https://doi.org/10.1016/j.eml.2020.101065

Wan, G., Liu, Y., Xu, Z., Jin, C., Dong, L., Han, X., Zhang, J.X.J., Chen, Z., 2019. Tunable bistability of a clamped elastic beam. Extreme Mechanics Letters 100603. https://doi.org/10.1016/j.eml.2019.100603

Wang, Y., Wang, Q., Liu, M., Qin, Y., Cheng, L., Bolmin, O., Alleyne, M., Wissa, A., Baughman, R.H., Vella, D., Tawfick, S., 2023. Insect-scale jumping robots enabled by a dynamic buckling cascade. Proceedings of the National Academy of Sciences 120, e2210651120. https://doi.org/10.1073/pnas.2210651120

Wani, O.M., Zeng, H., Priimagi, A., 2017. A light-driven artificial flytrap. Nat Commun 8, 15546. https://doi.org/10.1038/ncomms15546

Wiebe, R., Virgin, L.N., 2016. On the experimental identification of unstable static equilibria. Proceedings of the Royal Society A: Mathematical, Physical and Engineering Sciences 472, 20160172. https://doi.org/10.1098/rspa.2016.0172

Wu, L., Pasini, D., n.d. In-situ Activation of Snap-through Instability in Multi-response Metamaterials through Multistable Topological Transformation. Advanced Materials n/a, 2301109. https://doi.org/10.1002/adma.202301109

Xie, L., Liu, H., Yang, W., 2004. Adapting the nudged elastic band method for determining minimum-energy paths of chemical reactions in enzymes. The Journal of Chemical Physics 120, 8039–8052. https://doi.org/10.1063/1.1691404

Xiu, H., Liu, H., Poli, A., Wan, G., Sun, K., Arruda, E.M., Mao, X., Chen, Z., 2022. Topological transformability and reprogrammability of multistable mechanical metamaterials. Proceedings of the National Academy of Sciences 119, e2211725119. https://doi.org/10.1073/pnas.2211725119

Yan, W., Li, S., Deguchi, M., Zheng, Z., Rus, D., Mehta, A., 2023. Origami-based integration of robots that sense, decide, and respond. Nat Commun 14, 1553. https://doi.org/10.1038/s41467-023-37158-9

Yasuda, H., Korpas, L.M., Raney, J.R., 2020. Transition Waves and Formation of Domain Walls in Multistable Mechanical Metamaterials. Phys. Rev. Applied 13, 054067. https://doi.org/10.1103/PhysRevApplied.13.054067

Yasuda, H., Yang, J., 2015. Reentrant Origami-Based Metamaterials with Negative Poisson's Ratio and Bistability. Physical Review Letters 114. https://doi.org/10.1103/PhysRevLett.114.185502

Yu, T., Dreier, L., Marmo, F., Gabriele, S., Parascho, S., Adriaenssens, S., 2021. Numerical modeling of static equilibria and bifurcations in bigons and bigon rings. Journal of the Mechanics and Physics of Solids 152, 104459. https://doi.org/10.1016/j.jmps.2021.104459

Zhang, X., Wang, Y., Tian, Z., Samri, M., Moh, K., McMeeking, R.M., Hensel, R., Arzt, E., 2022. A bioinspired snap-through metastructure for manipulating micro-objects. Sci. Adv. 8, eadd4768. https://doi.org/10.1126/sciadv.add4768

Zhang, Y., Jiao, Y., Wu, J., Ma, Y., Feng, X., 2020. Configurations evolution of a buckled ribbon in response to out-of-plane loading. Extreme Mechanics Letters 34, 100604. https://doi.org/10.1016/j.eml.2019.100604

Zhao, Q., Yang, X., Ma, C., Chen, D., Bai, H., Li, T., Yang, W., Xie, T., 2016. A bioinspired reversible snapping hydrogel assembly. Mater. Horiz. 3, 422–428. https://doi.org/10.1039/C6MH00167J

Zhou, H., Grasinger, M., Buskohl, P., Bhattacharya, K., 2023. Low energy fold paths in multistable origami structures. International Journal of Solids and Structures 265–266, 112125. https://doi.org/10.1016/j.ijsolstr.2023.112125